

# Daytime urban heat stress in North America reduced by irrigation

Received: 5 March 2024

Accepted: 15 November 2024

Published online: 9 January 2025

 Check for updates

TC Chakraborty<sup>1</sup>✉, Yun Qian<sup>1</sup>✉, Jianfeng Li<sup>1</sup>, L. Ruby Leung<sup>1</sup> & Chandan Sarangi<sup>2,3</sup>

There is considerable uncertainty regarding the impact of irrigation on heat stress, partly stemming from the choice of heat stress index. Moreover, existing simulations are at scales that cannot appropriately resolve population centres or clouds and thus the potential for human impacts. Using multi-year convection-permitting and urban-resolving regional climate simulations, we demonstrate that irrigation alleviates summertime heat stress across more than 1,600 urban clusters in North America. This holds true for most physiologically relevant heat stress indices. The impact of irrigation varies by climate zone, with more notable irrigation signals seen for arid urban clusters that are situated near heavily irrigated fields. Through a component attribution framework, we show that irrigation-induced changes in wet-bulb temperature, often used as a moist heat stress proxy in the geosciences, exhibit an opposite sign to the corresponding changes in wet bulb globe temperature—a more complete index for assessing both indoor and outdoor heat risk—across climate zones. In contrast, the local changes in both wet-bulb and wet bulb globe temperature due to urbanization have the same sign. Our results demonstrate a complex relationship between irrigation and heat stress, highlighting the importance of using appropriate heat stress indices when assessing the potential for population-scale human impacts.

Irrigation is one of the most widespread land management practices<sup>1</sup> and is critical for sustaining modern food demand. The practice of irrigation strategically changes the water availability of agricultural lands, thereby modifying surface energy and moisture budgets<sup>1,2</sup>, with major impacts on regional climate<sup>3,4</sup>. Irrigation modulates the potential for heat risk by changing near-surface temperature and humidity<sup>4</sup> and through broader feedback<sup>2,5,6</sup>. The scientific discussion surrounding the role of irrigation in heat exposure has progressed from examining just air temperature changes<sup>7</sup> to quantification of moist heat stress changes through competing impacts of reduced temperature and increased humidity<sup>4,7,8</sup>.

Studies on irrigation impacts on moist heat stress have often focused on South Asia, which is a global hotspot for soil-moisture-induced climate feedback<sup>9</sup>. Whether irrigation increases or decreases

moist heat stress in this region has, however, been strongly debated, with conflicting results depending on model configuration and heat stress index used<sup>10–12</sup>. The latter issue is due to varying sensitivities of different heat stress indices to temperature and humidity<sup>12–14</sup>. Irrigation also modifies the climate of North America<sup>2,6</sup>, with large biases in simulated surface variables attributed to its poor representation in models<sup>15</sup>. Modelling studies of irrigation-induced heat stress use coarse grids<sup>10,11</sup>, with the implicit assumption that both the irrigation impact and human exposure to it can be represented appropriately at that scale. However, both irrigation and its intersection with human habitation are at substantially finer scales<sup>16</sup>. Of note, in North America, over 80% of people live in urban areas, which are rarely resolved in climate models<sup>17,18</sup>, and which also modulate local heat stress<sup>14</sup>. Heat stress is also strongly impacted by solar radiation,

<sup>1</sup>Pacific Northwest National Laboratory, Richland, WA, USA. <sup>2</sup>Department of Civil Engineering, IIT Madras, Chennai, India. <sup>3</sup>Geophysical Flows Lab, IIT Madras, Chennai, India. ✉e-mail: [tc.chakraborty@pnnl.gov](mailto:tc.chakraborty@pnnl.gov); [yun.qian@pnnl.gov](mailto:yun.qian@pnnl.gov)

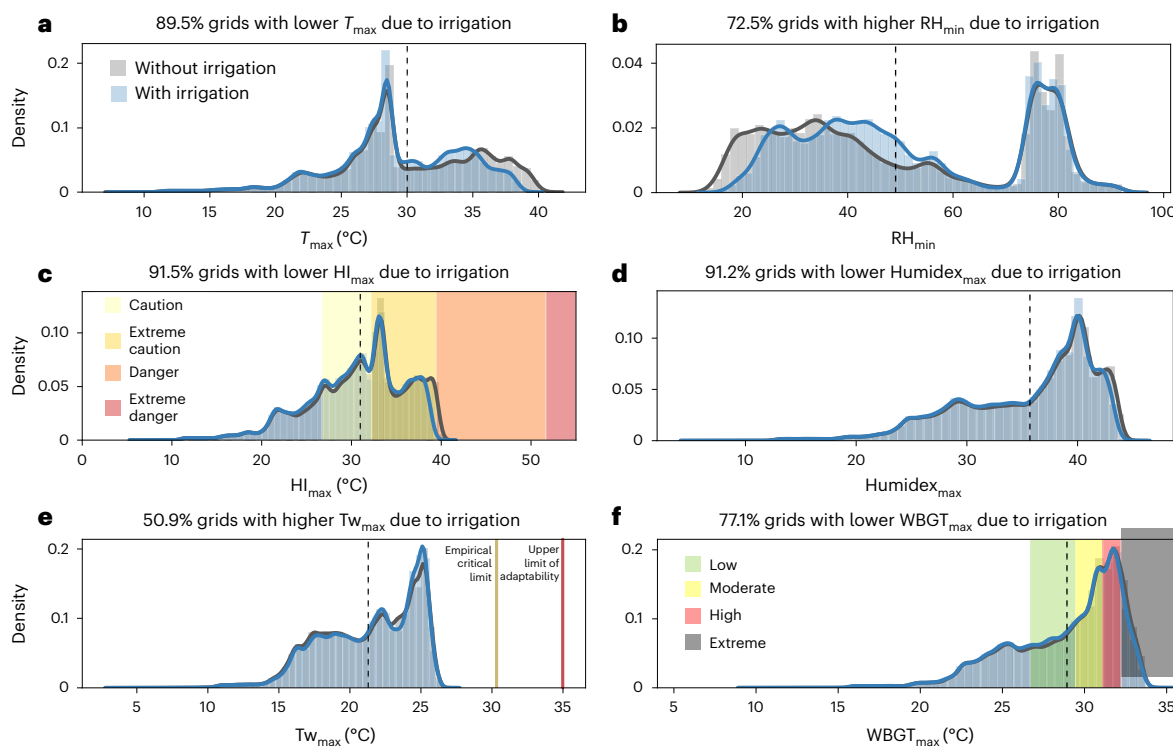


**Fig. 1 | Distribution of grid-averaged daytime surface climate and heat stress.**

**a–f**, Probability density distributions of grid-averaged average maximum air temperature ( $T_{\max}$ ) (**a**), average minimum relative humidity ( $\text{RH}_{\min}$ ) (**b**), average maximum heat index ( $\text{HI}_{\max}$ ) (**c**), average maximum Humidex ( $\text{Humidex}_{\max}$ ) (**d**), average maximum wet-bulb temperature ( $\text{Tw}_{\max}$ ) (**e**) and average maximum wet bulb globe temperature ( $\text{WBGT}_{\max}$ ) (**f**) with and without irrigation. The vertical

black dashed lines represent mean values and the percentage of grids showing irrigation-induced changes is noted. The spatial plots of changes in these variables are in Extended Data Figs. 3 and 5 and Supplementary Information. Heat risk categories used by the US National Weather Service are marked for  $\text{HI}$  and  $\text{WBGT}$  (**c** and **f**). For **e**, the upper limit of human adaptability for  $\text{Tw}$  and a lower empirically determined limit (Methods) are marked.

and resolving irrigation-induced changes to it requires fine-scale model simulations<sup>6,19</sup>.

Here we use multi-year convection-permitting and urban-resolving regional climate simulations covering most of North America to demonstrate that irrigation, specifically agricultural irrigation (Supplementary Fig. 1a), reduces summertime heat stress over most urban clusters in the region (Extended Data Fig. 1). The sign of the change is consistently seen for multiple heat stress indices commonly used in the scientific literature. However, the magnitudes of both irrigation and urbanization impacts depend on the heat stress index used. We further perform a component attribution of the wet bulb globe temperature, a comprehensive heat stress index that considers temperature, humidity, wind speed and radiation, to discuss the discrepancies between implicit regional modelling assumptions of heat exposure and the potential for real indoor and outdoor population-scale heat risk.

## Irrigation impacts on surface climate and heat stress

Comparing simulations with and without irrigation, we find irrigation-induced decrease and increase in sensible ( $H$ ) and latent heat fluxes ( $\lambda E$ ), respectively, during summer (Supplementary Fig. 2g,h), even though incoming solar radiation ( $K_{\downarrow}$ ) barely changes (Supplementary Fig. 2f). Even with no change in forcing, a decrease in the Bowen ratio ( $\frac{H}{\lambda E}$ ) would lead to evaporative cooling<sup>20</sup>, while the increase in  $\lambda E$  would add more moisture into the near-surface air. However, there are other adjustments to the surface energy budget that also modulate the response of the climate system to the simulated irrigation. For instance, the surface cooling reduces the outgoing longwave feedback (Extended Data Fig. 2a), which, in turn, increases the net absorbed

energy by the surface (Extended Data Fig. 2b), partially counteracting that cooling. Overall, irrigation reduces maximum and minimum air temperature ( $T$ ) and increases the corresponding relative humidity (RH) (Supplementary Figs. 1–4 and Methods). The irrigation cooling effect during daytime (corresponding to maximum  $T$ , referred to as  $\Delta T_{\max}$ ) is larger than that ( $\Delta T_{\min}$ ; irrigation-induced change corresponding to  $T_{\min}$ ) at night (Supplementary Figs. 3a and 4a). This day–night asymmetry may be because  $\Delta T_{\min}$  is moderated through the reduction in the longwave cooling (Extended Data Fig. 2a), which is the primary heat dissipation mechanism at night. Less day–night asymmetry is seen for the irrigation impact on RH ( $\Delta \text{RH}$ ; Supplementary Figs. 3b and 4b). For both day and night, there are large spatial variabilities in the irrigation impacts on  $T$  and RH, with hotspots in the Midwest, which are heavily irrigated regions<sup>15</sup>, and parts of the US Southeast. Increases in both  $T$  and RH would enhance moist heat stress<sup>13,21</sup>. The competing impacts of lower  $T_{\max}$  and higher  $\text{RH}_{\min}$  (RH is generally minimum when  $T$  is maximum during the diurnal cycle) tend to reduce daytime moist heat stress, seen for around 91% of the model grids (Fig. 3c,d) for both maximum heat index ( $\text{HI}_{\max}$ ) and Humidex ( $\text{Humidex}_{\max}$ ). As an example, the percentage of grids with  $\text{HI}_{\max}$  in the ‘Danger’ category, as defined by the US National Weather Service (NWS), decreases from 1.39% to around 0.02% due to irrigation (Fig. 1c). Although irrigation-induced reductions in  $\text{Humidex}_{\max}$  are evident, the magnitude of change is smaller than for  $\text{HI}_{\max}$  and larger increases are seen in the Midwest at night (Supplementary Fig. 4d). This is because of the higher sensitivity to RH for Humidex than for  $\text{HI}$ <sup>12,13,22</sup>.

## Influence of irrigation on urban moist heat stress

When we aggregate the irrigation impacts for over 1,600 urban clusters, the results are similar with the domain-wide results, with decreases in  $T_{\max}$ ,  $\text{HI}_{\max}$  and  $\text{Humidex}_{\max}$  and increases in  $\text{RH}_{\min}$  (Fig. 2). The overall

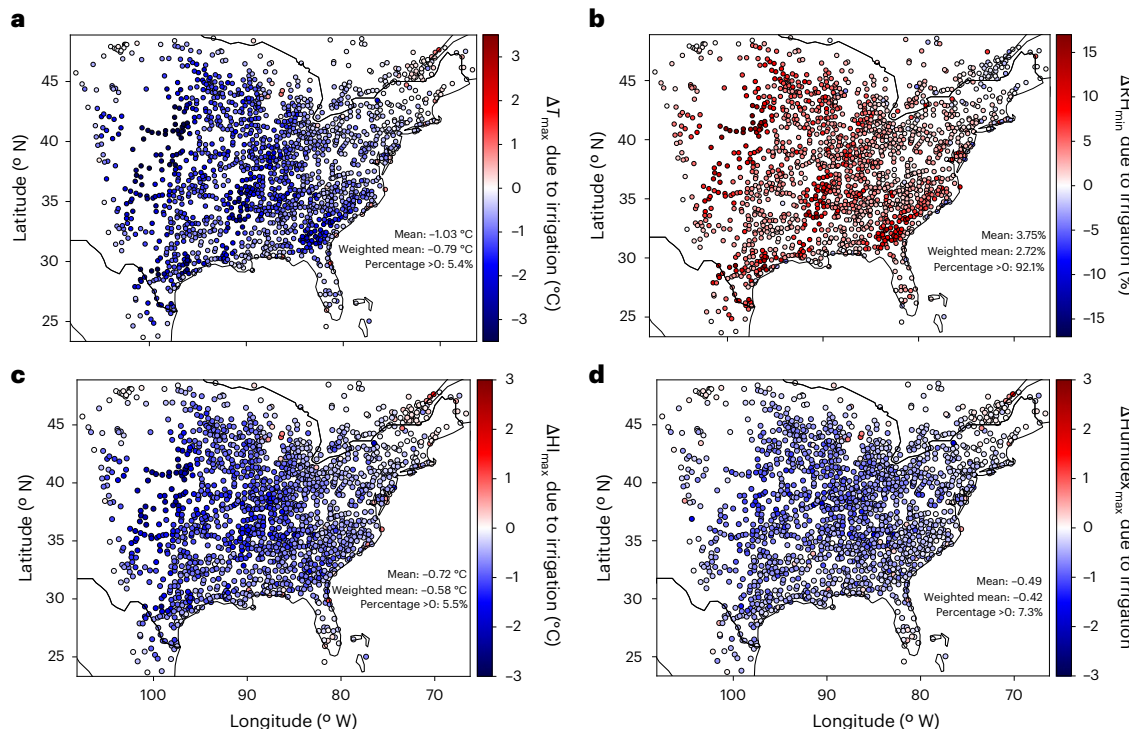


**Fig. 2 | Irrigation-induced changes in daytime urban climate and moist heat stress.** **a–d**, Irrigation-induced urban-scale changes in maximum air temperature ( $\Delta T_{\max}$ ) (a), minimum relative humidity ( $\Delta RH_{\min}$ ) (b), maximum heat index ( $\Delta HI_{\max}$ ) (c) and maximum Humidex ( $\Delta \text{Humidex}_{\max}$ ) (d) for every urban cluster

in the model domain. Each dot represents an urban cluster. The spatial means, area-weighted spatial means and percentage of urban clusters with values above 0 are noted.

area-weighted mean irrigation-induced urban  $T_{\max}$  reduction is 0.79 °C and the corresponding  $RH_{\min}$  increase is 2.72%. Similarly, urban  $HI_{\max}$  and  $\text{Humidex}_{\max}$  are reduced by 0.58 °C and 0.42 (Humidex is unitless), respectively. The percentage of urban clusters with irrigation-induced cooling and moistening is greater than the percentage seen for the model grids (94.6% versus 89.5% for  $T_{\max}$  and 92.1% versus 72.5% for  $RH_{\min}$ ; Figs. 1 and 2). The difference between these two values illustrates the importance of resolving urban centres, where most people live, instead of using regional climate simulations that ignore urban-scale processes, the latter being common in irrigation impact studies<sup>10,11</sup>. Irrigation also reduces minimum urban moist heat stress, though a larger fraction of the clusters shows increases in  $HI_{\min}$  and  $\text{Humidex}_{\min}$  at night (Extended Data Fig. 3) compared to the changes seen during daytime (Fig. 2). The changes in the surface climate and heat stress estimates are smaller when the areas of the urban clusters are accounted for in most cases (comparing the means and area-weighted means in Fig. 2 and Extended Data Fig. 3). This can be attributed to smaller impacts of irrigation on larger urban clusters that are farther away from the major agricultural regions and in coastal areas (for instance, in the Northeast and the South; Extended Data Fig. 1 and Fig. 2).

## Impacts by climate zone

The study region and the urban clusters within it can be grouped into four climate zones<sup>23</sup>, namely arid, boreal, temperate and tropical (Extended Data Fig. 1). Given the small sample size of tropical urban clusters ( $n = 8$ ), most of which are also coastal, it is difficult to get robust and definitive irrigation signals for them. As such, the overall results below primarily refer to arid, boreal and temperate climate zones. Some clear differences are seen in the irrigation impacts by background climate, with the arid urban clusters showing stronger irrigation-induced cooling and moistening than in any of the other cases. Irrigation increases the  $RH_{\min}$  in 96.5% of the 86 arid urban clusters (Fig. 3b). These larger impacts in arid zones are partly due to the proximity of these clusters

to croplands that depend strongly on heavy irrigation (Supplementary Fig. 1a). In arid regions, evapotranspiration tends to be more sensitive to soil moisture, and thus irrigation<sup>24</sup>, which is reflected in the larger percentage changes in both  $H$  and  $\lambda E$  (Supplementary Fig. 2g,h). Due to the compensating effects of lower  $T$  and higher RH, the dependence of the irrigation impacts on climate zone is lower for moist heat stress. While irrigation-induced  $HI_{\max}$  reduction is greatest for arid urban clusters, the reduction in  $\text{Humidex}_{\max}$  is among the lowest (Fig. 3). During nighttime, there is little difference in irrigation-induced cooling across climate zones, whereas  $RH_{\max}$  is enhanced the most in the arid urban clusters (Extended Data Fig. 4). For minimum moist heat stress, there is similarly little difference by climate zone. The main exception is for arid clusters, where irrigation-induced increase in Humidex is seen (Extended Data Fig. 4d).

## Examining contributions to outdoor heat stress

Humidex and HI are both operational heat stress indices used by the Meteorological Service of Canada and the US NWS, respectively. Another variable that has been often used to examine moist heat stress is the wet-bulb temperature ( $T_w$ ), which we also consider here (Fig. 1e and Extended Data Fig. 5). Much of the scientific debate surrounding the impact of irrigation on heat stress is rooted in the choice of moist heat stress index and their different sensitivities to temperature and humidity<sup>10–13</sup>. However, most of these indices only consider the impact of temperature and humidity on heat stress and ignore solar radiation and wind speed (WS), both of which modify the human body's energy budget and thus potential for heat loading<sup>25</sup>. Thus, we also consider the irrigation-induced change in a more complete heat stress index, namely the wet bulb globe temperature (WBGT). The outdoor WBGT can be written as a linear combination of  $T$  (or dry-bulb temperature),  $T_w$  (natural wet-bulb temperature) and black-globe temperature ( $T_g$ ):

$$\text{WBGT} = 0.1 \times T + 0.7 \times T_w + 0.2 \times T_g \quad (1)$$

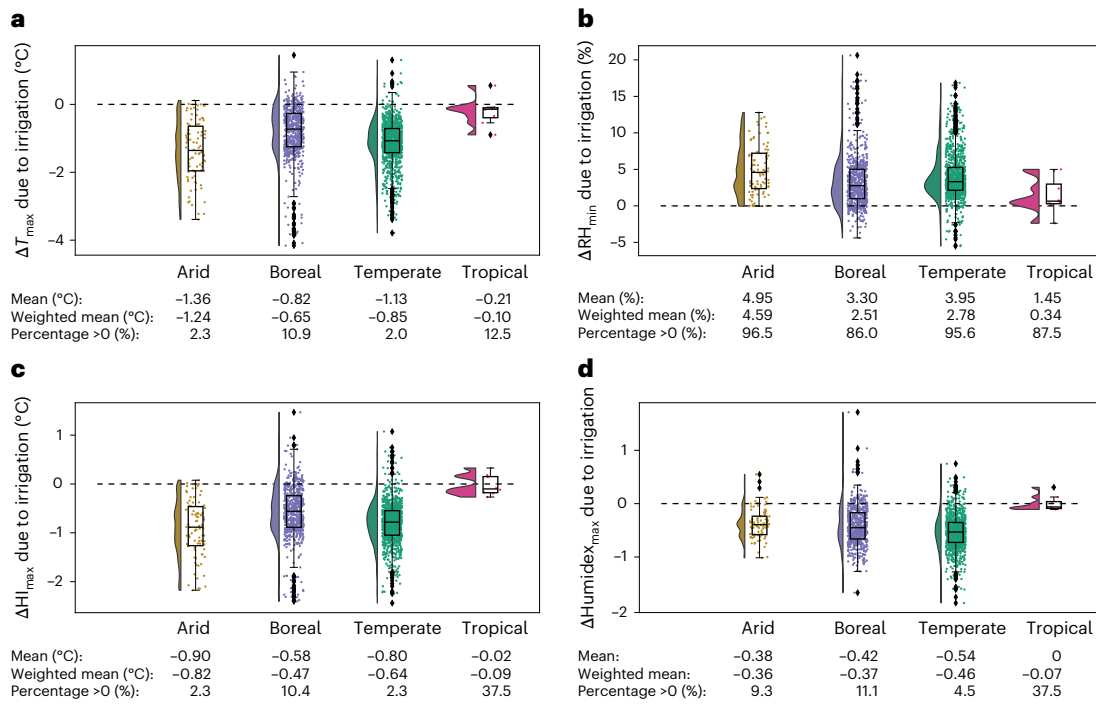


**Fig. 3 | Daytime irrigation impacts on urban climate and moist heat stress across climate zones.** **a–d**, Distribution of irrigation-induced changes in maximum air temperature ( $\Delta T_{\max}$ ) (a), minimum relative humidity ( $\Delta RH_{\min}$ ) (b), maximum heat index ( $\Delta HI_{\max}$ ) (c) and maximum Humidex ( $\Delta \text{Humidex}_{\max}$ ) (d) for every urban cluster in the model domain by climate zone. The means, area-weighted means and percentage of urban clusters with values above 0 are

noted for each case. Each dot represents the spatial mean for an urban cluster. The number of clusters in arid, boreal, temperate and tropical climate are 86, 605, 961 and 8, respectively. The boxes range from the first to third quartile of the subsets of data, with the median marked by a line. The whiskers extend to 1.5 times the interquartile ranges of the boxes.

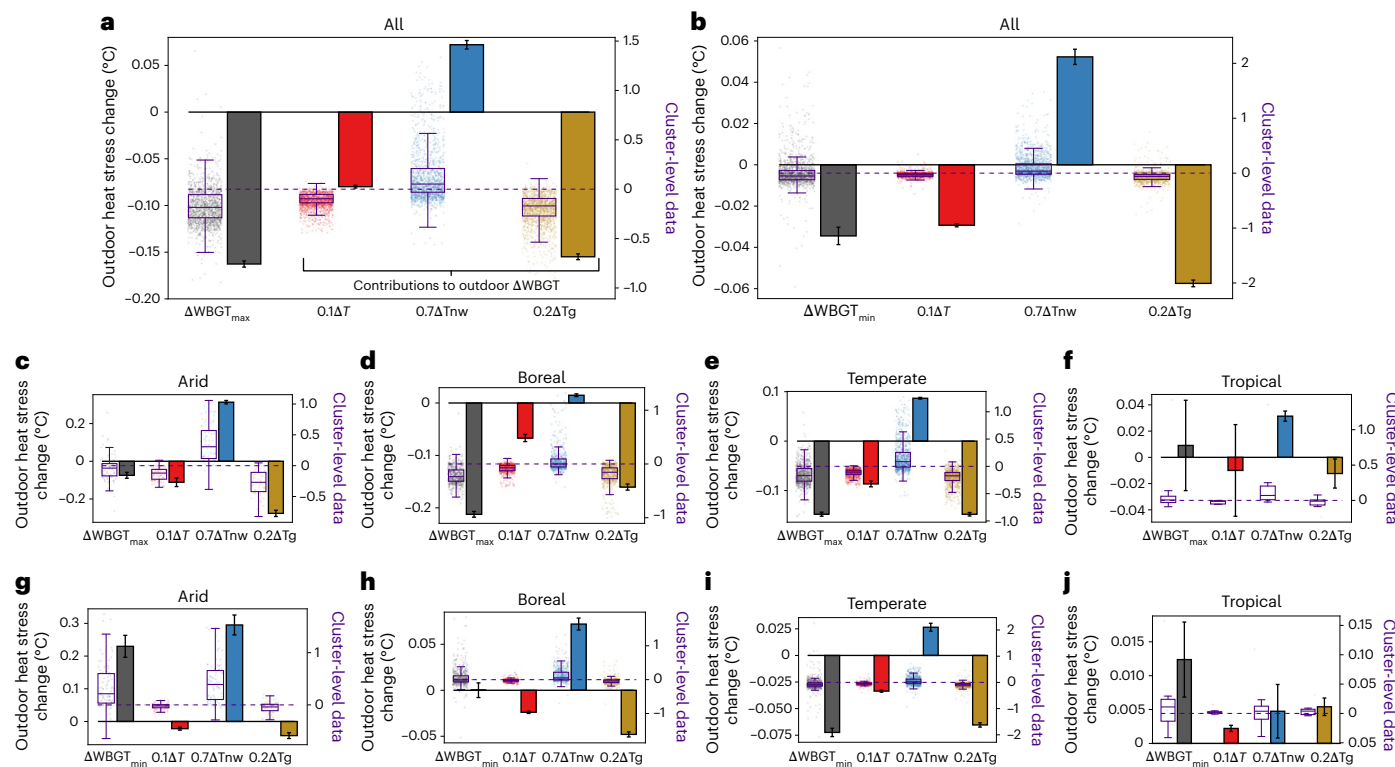


**Fig. 4 | Changes in urban outdoor wet bulb globe temperature and its components due to irrigation.** **a,b**, Irrigation-induced changes in average maximum (a) and minimum (b) outdoor wet bulb globe temperature ( $\Delta WBGT_{\max}$  and  $\Delta WBGT_{\min}$ , respectively) in urban clusters. **c–f**, Similar to a (for  $\Delta WBGT_{\max}$ ) but for arid, boreal, temperate and tropical urban clusters, respectively. **g–j**,  $\Delta WBGT_{\min}$  by climate zone. The contributions of change in dry-bulb or air temperature ( $\Delta T$ ), natural wet-bulb temperature ( $\Delta T_{nw}$ ) and black-globe

temperature ( $\Delta T_g$ ) are shown. The bars represent area-weighted means, and the error bars show area-weighted standard errors. The distributions of the cluster-level data and the associated box and whisker plots correspond to the right-hand y-axis range. The number of clusters in arid, boreal, temperate and tropical climate are 86, 605, 961 and 8, respectively. The boxes range from the first to third quartile of the subsets of data, with the median marked by a line. The whiskers extend to 1.5 times the interquartile ranges of the boxes.

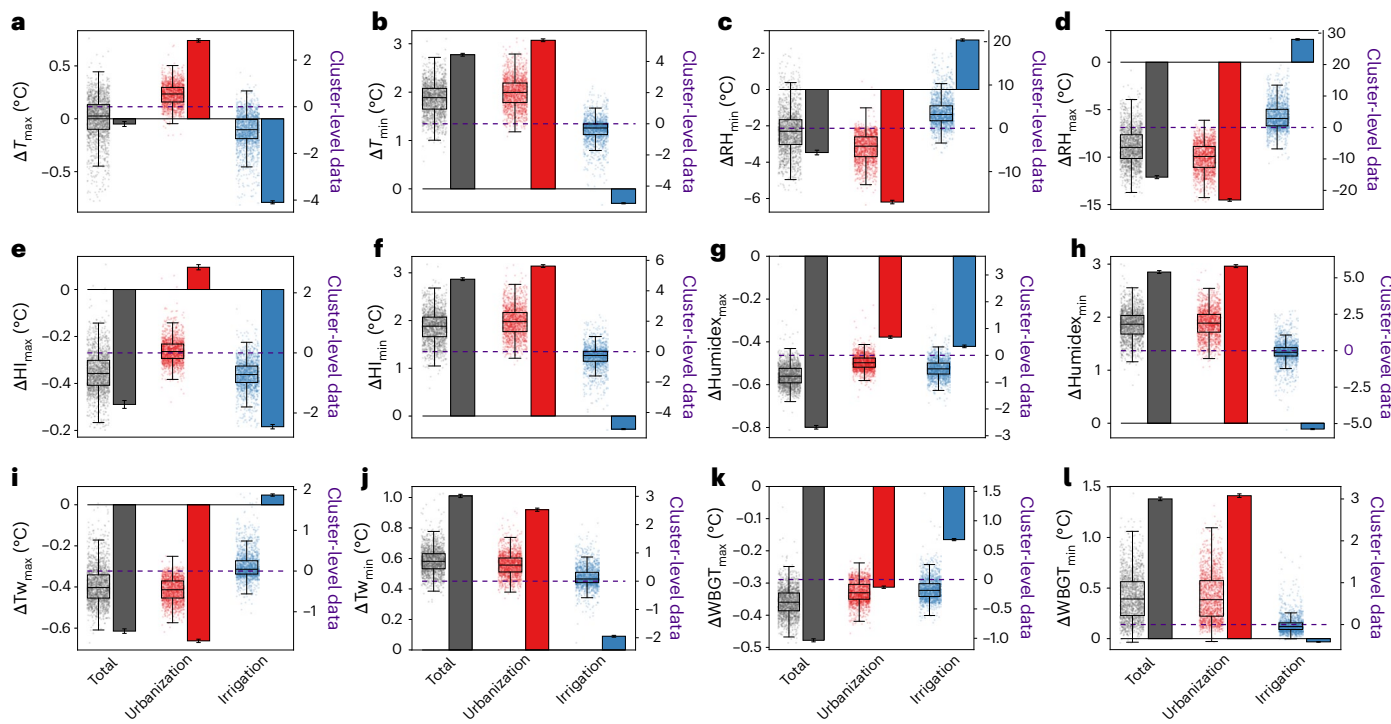


**Fig. 5 | Impacts of urbanization versus irrigation.** **a–l**, Irrigation- and urbanization-induced changes in maximum air temperature ( $\Delta T_{\max}$ ) (a), relative humidity ( $\Delta RH_{\max}$ ) (c), heat index ( $\Delta HI_{\max}$ ) (e), Humidex ( $\Delta \text{Humidex}_{\max}$ ) (g), wet-bulb temperature ( $\Delta Tw_{\max}$ ) (i), wet bulb globe temperature ( $\Delta WBGT_{\max}$ ) (k) and minimum air temperature ( $\Delta T_{\min}$ ) (b), relative humidity ( $\Delta RH_{\min}$ ) (d), heat index ( $\Delta HI_{\min}$ ) (f), Humidex ( $\Delta \text{Humidex}_{\min}$ ) (h), wet-bulb temperature ( $\Delta Tw_{\min}$ ) (j) and wet bulb globe temperature ( $\Delta WBGT_{\min}$ ) (l) for urban clusters in the model domain. The total changes represent the combined effects of both. The bars

represent area-weighted means and the error bars show area-weighted standard errors. The distributions of the cluster-level data and the associated box and whisker plots correspond to the right-hand y axis range. The number of clusters in arid, boreal, temperate and tropical climate are 86, 605, 961 and 8, respectively. The boxes range from the first to third quartile of the subsets of data, with the median marked by a line. The whiskers extend to 1.5 times the interquartile ranges of the boxes.

WBGT is the International Organization for Standardization standard for occupational heat stress<sup>26</sup> and performs the best at explaining physiological heat strain<sup>27</sup>, with both its Tg and Tnw components explicitly accounting for the impact of  $K_{\downarrow}$  and WS.

On average, irrigation-induced reductions in both  $WBGT_{\max}$  and  $WBGT_{\min}$  are seen over urban areas, with larger reductions for  $WBGT_{\max}$  (Fig. 4a,b). Results are consistent across climate zones (and also for several other approximations of WBGT; Extended Data Fig. 6), with exceptions for  $WBGT_{\min}$  over boreal urban clusters (Fig. 4h), with negligible changes, and for arid urban clusters (Fig. 4g), where  $WBGT_{\min}$  increases. When separating the contributions to  $\Delta WBGT$ , the concurrent  $\Delta T$  and  $\Delta T_g$  tend to reduce it, whereas  $\Delta T_{nw}$  increases it. Although the weight for  $T_g$  is smaller than for  $T_{nw}$  in equation 2, it has a larger range of values than  $T_{nw}$ <sup>28</sup>. These large irrigation-induced reductions in  $T_g$  occur even though  $K_{\downarrow}$  shows no major change and WS decreases (Extended Data Fig. 7), which would increase heat stress, all else being equal. This is because  $T$  and its changes are strongly baked into  $T_g$  (equations (9) and (10) in Methods) and thus into WBGT. This can be illustrated by representing the spatial variability of  $WBGT_{\max}$  as a multilinear equation of all its inputs ( $T$ , absolute humidity or AH,  $K_{\downarrow}$  and WS; all scaled for easy comparison), with  $T$  showing the highest regression coefficient (1.12). Note that the spatial variabilities in  $\Delta K_{\downarrow}$  (Extended Data Fig. 7b) are strongly linked with changes in cloud fraction (Extended Data Fig. 8b). This demonstrates the importance of convection-permitting simulations when examining large-scale irrigation-induced feedback, also seen for precipitation systems over this region<sup>6</sup>, with implications for WBGT. There are several other changes due to irrigation in this coupled framework. For instance, we find a general reduction in the planetary boundary layer height due to irrigation (Extended Data Fig. 9a), which is

strongly associated with  $\Delta Tw_{\max}$  (Extended Data Fig. 9b) and consistent with global-scale analyses using coarser reanalysis data<sup>29</sup>.

### Impacts of urbanization versus irrigation

Urbanization generally increases local  $T$ , the urban heat island effect, and reduces RH, the urban dry island effect, with these competing changes affecting local heat stress<sup>14</sup>. Many studies have focused on this local impact of urbanization on heat stress<sup>17,30–34</sup>. Similar to the discussions surrounding irrigation, the scientific focus has recently switched to moist heat stress indices at these scales. With the intent of better examining urban heat stress, we use a third set of simulations with urban land removed to compare the urbanization and irrigation impacts on various heat stress indices. Whereas irrigation mainly reduces urban heat stress, the impact of urbanization is mixed, with urbanization increasing nighttime heat stress and generally decreasing daytime heat stress. The only exception is seen for  $HI_{\max}$ , which increases due to urbanization (Fig. 5e). That urbanization reduces or barely impacts daytime heat stress goes against standard discourse on additional impact of urbanization on local heat stress, which frequently focuses on daytime conditions, but is consistent with previous observation results<sup>14</sup>. The urban impacts on  $T$ , RH and heat stress indices at night are individually larger over urban areas than the impact of irrigation (Fig. 5b,d,f,h,j,l). For daytime (rather, maximum values), the impact of urbanization can be more or less than that for irrigation depending on the variable. Finally, while the focus here was on the local impact of urbanization and the regional impact of irrigation on local urban heat stress, urbanization may also modify regional climate through various mechanisms<sup>35–38</sup>. Such regional urban impacts may become increasingly important as cities grow and evolve in the future<sup>39</sup>.

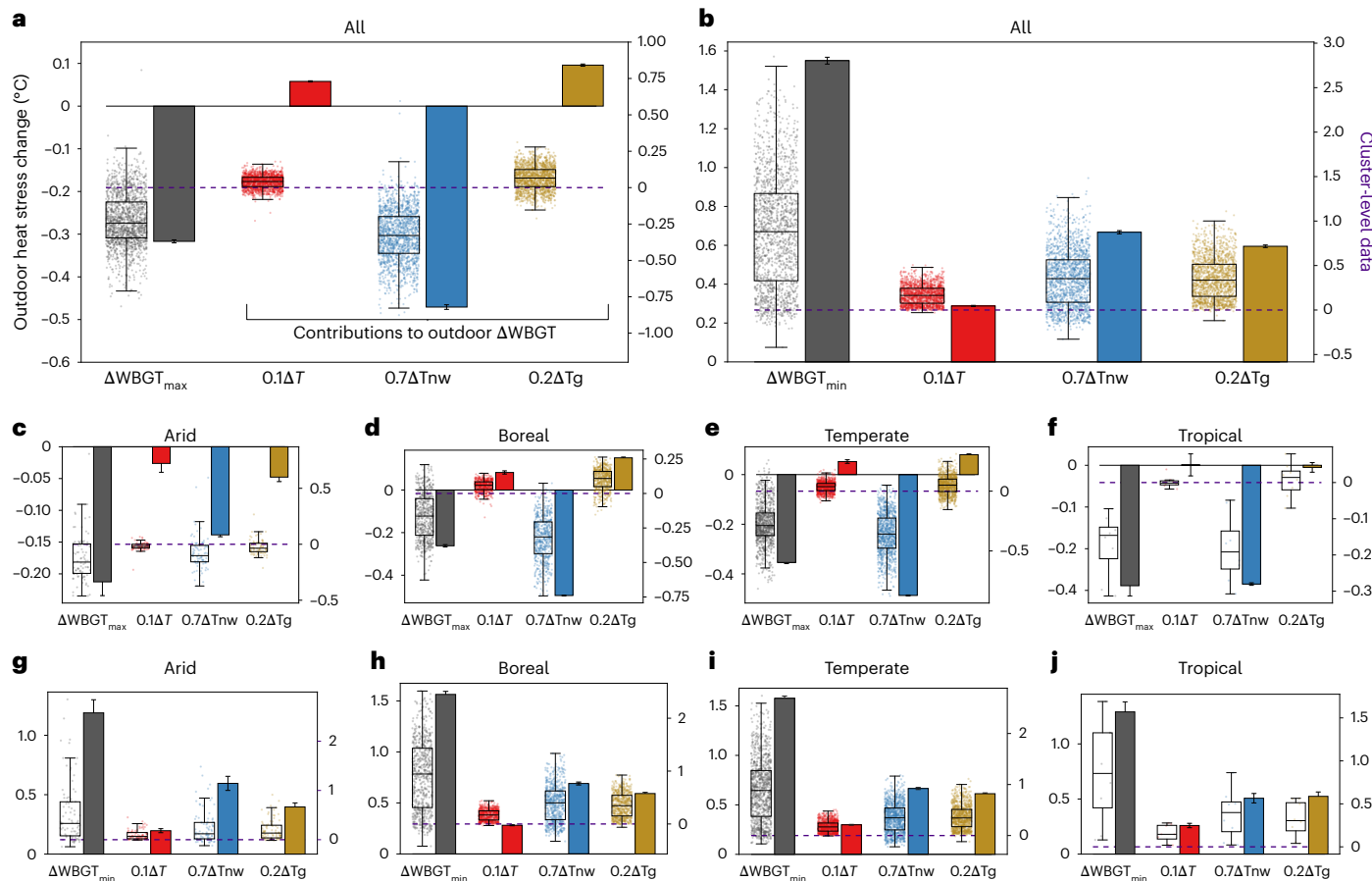


**Fig. 6 | Changes in urban outdoor wet bulb globe temperature and its components due to urbanization.** **a,b**, Urbanization-induced changes in average maximum (**a**) and minimum (**b**) outdoor wet bulb globe temperature ( $\Delta\text{WBGT}_{\text{max}}$  and  $\Delta\text{WBGT}_{\text{min}}$ , respectively) in urban clusters. **c–f**, Similar to **a** (for  $\Delta\text{WBGT}_{\text{max}}$ ), but for arid, boreal, temperate and tropical urban clusters, respectively. **g–j**, Similarly,  $\Delta\text{WBGT}_{\text{min}}$  by climate zone. The contributions of change in dry-bulb or air temperature ( $\Delta T$ ), natural wet-bulb temperature ( $\Delta\text{Tnw}$ ) and

black-globe temperature ( $\Delta\text{Tg}$ ) are shown. The bars represent area-weighted means, and the error bars show area-weighted standard errors. The distributions of the cluster-level data and the associated box and whisker plots correspond to the right-hand y axis range. The number of clusters in arid, boreal, temperate and tropical climate are 86, 605, 961 and 8, respectively. The boxes range from the first to third quartile of the subsets of data, with the median marked by a line. The whiskers extend to 1.5 times the interquartile ranges of the boxes.

## Role of choice of heat stress index on results

Impacts of land use and land management practices, such as urbanization and irrigation, on physiologically relevant heat stress can be difficult to isolate due to the number of factors involved, choice of variables and methodological uncertainties. An index that is commonly used in the geosciences as a proxy for heat stress is the psychrometric or thermodynamic wet-bulb temperature  $T_w$ <sup>10,17,21,33,40–42</sup>. Although  $T_w$  does not always linearly correspond to health outcomes<sup>43</sup> and ranks towards the bottom of thermal stress indicators for explaining variance in physiological heat strain (WBGT ranks at the top, and both Humidex and HI are close to the top)<sup>27</sup>, it being a thermodynamic variable derivable from first principles makes it conceptually simple to diagnose and attribute<sup>33,44</sup>. Moreover, some physiological studies have indeed shown impacts of  $T_w$  on heat stress beyond specific thresholds (Fig. 1e)<sup>45</sup>. However,  $T_w$  is also commonly used at values lower than these thresholds to understand the direction of change due to various perturbations to the climate system<sup>9,10,12,17,33,40</sup>. For irrigation, we find that the direction of the change in  $T_w$  does not correspond to the change in WBGT (Fig. 4), the latter being a more effective indicator of physiological heat strain under both indoor and outdoor conditions<sup>27</sup>. For the natural wet-bulb temperature  $\text{Tnw}$ , which also includes the impact of  $K_v$  and WS and is a component of WBGT, its irrigation-induced change also shows an opposite sign from the change in WBGT in most cases (Fig. 5).

On the other hand, for urbanization, the signs of  $\Delta\text{Tnw}$  and  $\Delta\text{WBGT}$  are consistent (Fig. 6).

## Assessing realistic potential for human exposure

The solar radiation and wind speed at 4 km, used in the WBGT calculation, would not sufficiently resolve urban-scale heat hazard due to large variabilities in morphology and shade structures<sup>46</sup>. This is an example of a somewhat common spatiotemporal incoherence in studies that link model-simulated heat stress indices to human impacts. This is partly due to the coarse model resolutions used in many studies<sup>10,11,17</sup>. There are large spatial variabilities within model grids that are relevant for both human exposure, such as those within urban areas<sup>22</sup>, and for regional climate feedback, including from irrigation (Extended Data Fig. 8)<sup>6</sup>. Climate models, for instance, do not consider the location of different surface types within a model grid, thus only calculate one-dimensional interactions between the atmosphere and biosphere within sometimes a hundred kms or more<sup>17</sup>. Doing so misses important gradients relevant for heat exposure, such as from rural to urban areas and across other land-cover transitions<sup>38</sup>. In our convection-permitting and urban-resolving simulations, we observe a discrepancy between the number of model grids and urban clusters experiencing irrigation-induced reduction in moist heat stress. This discrepancy arises from the spatial distribution of urban areas in

relation to the regular model grids (Figs. 1 and 2, Supplementary Fig. 2 and Extended Data Fig. 1).

Other major sources of incoherence stem from simplistic assumptions used to link climate-scale variables to potential for human impacts<sup>25</sup>. When quantifying impacts due to climate change, urbanization or irrigation, there is an implicit assumption that the majority of the residents in the study region would be exposed to these extremes. This is not a reasonable assumption, especially in urban areas, where people spend most of their time indoors, especially during the warmest times of the day. Using an indoor estimate of WBGT, where we reduce both  $K_a$  and WS to zero and modify equation (2), we still find irrigation-induced reductions in WBGT (Extended Data Fig. 10). This kind of estimate assumes that the outdoor climate ( $T$  and RH) and indoor climate are identical, which is also incorrect due to various factors, from air conditioning use to building insulation. These factors relate to population-scale vulnerability to heat, modulating overall heat risk. The common use of  $T_w$  thresholds to quantify extreme heat risks also follow these somewhat ideal assumptions, with potential for both over and under estimations compared to the real environment. The upper adaptability limit of  $T_w$  of 35 °C is based on an idealistic model of the human body. Quoting Sherwood and Huber<sup>44</sup>, “Our limit applies to a person out of the sun, in gale-force winds, doused with water, wearing no clothing and not working.” Intuitively, these assumptions are rarely relevant for indoor or outdoor conditions. In indoor conditions, gale-force winds are generally impossible, and the ambient  $T$  and RH cannot simply be sourced from outdoor climatological signals. In outdoor environments, the adaptability limit would be lower than 35 °C due to more heat needing to be dissipated in active conditions and due to strong impact of solar radiation on heat loading<sup>25</sup>. However, we would only expect a small fraction of the population of a grid to be outdoors during the peak heat stress hours.

In summary, although examining heat stress signals is crucial for understanding the effects of climate perturbations on the potential for heat exposure, one should be cautious when directly attributing those signals to population-scale impacts. Evidently, this is true not only for  $T_w$ , a frequently used index in the geosciences<sup>10,21,44</sup>, but also for other more physiologically relevant indicators of heat stress and even the use of only  $T$  to predict mortality/morbidity risks<sup>47</sup>. A more constructive approach may involve defining scenarios of heat exposure that consider realistic levels of activity and exposure to indoor versus outdoor environments.

## Online content

Any methods, additional references, Nature Portfolio reporting summaries, source data, extended data, supplementary information, acknowledgements, peer review information; details of author contributions and competing interests; and statements of data and code availability are available at <https://doi.org/10.1038/s41561-024-01613-z>.

## References

- McDermid, S. et al. Irrigation in the Earth system. *Nat. Rev. Earth Environ.* **4**, 435–453 (2023).
- Qian, Y., Huang, M., Yang, B. & Berg, L. K. A modeling study of irrigation effects on surface fluxes and land-air-cloud interactions in the southern Great Plains. *J. Hydrometeorol.* **14**, 700–721 (2013).
- Sacks, W. J., Cook, B. I., Buenning, N., Levis, S. & Helkowski, J. H. Effects of global irrigation on the near-surface climate. *Clim. Dyn.* **33**, 159–175 (2009).
- Krakauer, N. Y., Cook, B. I. & Puma, M. J. Effect of irrigation on humid heat extremes. *Environ. Res. Lett.* **15**, 094010 (2020).
- Kawase, H. et al. Impact of extensive irrigation on the formation of cumulus clouds. *Geophys. Res. Lett.* **35**, L01806 (2008).
- Li, J. et al. Impacts of large-scale urbanization and irrigation on summer precipitation in the Mid-Atlantic region of the United States. *Geophys. Res. Lett.* **49**, e2022GL097845 (2022).
- Thiery, W. et al. Present-day irrigation mitigates heat extremes. *J. Geophys. Res. Atmos.* **122**, 1403–1422 (2017).
- Lobell, D. B., Bonfils, C. J., Kueppers, L. M. & Snyder, M. A. Irrigation cooling effect on temperature and heat index extremes. *Geophys. Res. Lett.* **35**, L09705 (2008).
- Koster, R. D. et al. Regions of strong coupling between soil moisture and precipitation. *Science* **305**, 1138–1140 (2004).
- Mishra, V. et al. Moist heat stress extremes in India enhanced by irrigation. *Nat. Geosci.* **13**, 722–728 (2020).
- Jha, R., Mondal, A., Devanand, A., Roxy, M. K. & Ghosh, S. Limited influence of irrigation on pre-monsoon heat stress in the Indo-Gangetic Plain. *Nat. Commun.* **13**, 4275 (2022).
- Simpson, C. H., Brousse, O., Ebi, K. L. & Heaviside, C. Commonly used indices disagree about the effect of moisture on heat stress. *npj Clim. Atmos. Sci.* **6**, 78 (2023).
- Sherwood, S. C. How important is humidity in heat stress?. *J. Geophys. Res. Atmos.* **123**, 11808–11810 (2018).
- Chakraborty, T., Venter, Z. S., Qian, Y. & Lee, X. Lower urban humidity moderates outdoor heat stress. *AGU Adv.* **3**, e2022AV000729 (2022).
- Qian, Y. et al. Neglecting irrigation contributes to the simulated summertime warm-and-dry bias in the central United States. *npj Clim. Atmos. Sci.* **3**, 31 (2020).
- Cooney, C. M. *Downscaling Climate Models: Sharpening the Focus on Local-Level Changes* (National Institute of Environmental Health Sciences, 2012).
- Zhao, L. Global multi-model projections of local urban climates. *Nat. Clim. Change* **11**, 152–157 (2021).
- Sharma, A., Wuebbles, D. J. & Kotamarthi, R. The need for urban-resolving climate modeling across scales. *AGU Adv.* **2**, e2020AV000271 (2021).
- Slingo, J. et al. Ambitious partnership needed for reliable climate prediction. *Nat. Clim. Change* **12**, 499–503 (2022).
- Chakraborty, T. C., Lee, X. & Lawrence, D. M. Strong local evaporative cooling over land due to atmospheric aerosols. *J. Adv. Model. Earth Syst.* **13**, e2021MS002491 (2021).
- Raymond, C., Matthews, T. & Horton, R. M. The emergence of heat and humidity too severe for human tolerance. *Sci. Adv.* **6**, eaaw1838 (2020).
- Chakraborty, T. C., Newman, A. J., Qian, Y., Hsu, A. & Sheriff, G. Residential segregation and outdoor urban moist heat stress disparities in the United States. *One Earth* **6**, 738–750 (2023).
- Rubel, F. & Kottek, M. Observed and projected climate shifts 1901–2100 depicted by world maps of the Köppen–Geiger climate classification. *Meteorol. Z.* **19**, 135–141 (2010).
- Dirmeyer, P. A., Balsamo, G., Blyth, E. M., Morrison, R. & Cooper, H. M. Land-atmosphere interactions exacerbated the drought and heatwave over northern Europe during summer 2018. *AGU Adv.* **2**, e2020AV000283 (2021).
- Vanos, J. et al. A physiological approach for assessing human survivability and liveability to heat in a changing climate. *Nat. Commun.* **14**, 7653 (2023).
- ISO 7243: *Ergonomics of the Thermal Environment—Assessment of Heat Stress Using the WBGT (Wet Bulb Globe Temperature) Index* (ISO, 2017).
- Ioannou, L. G. et al. Indicators to assess physiological heat strain—Part 3: Multi-country field evaluation and consensus recommendations. *Temperature* **9**, 274–291 (2022).
- Lemke, B. & Kjellstrom, T. Calculating workplace WBGT from meteorological data: a tool for climate change assessment. *Ind. Health* **50**, 267–278 (2012).

29. Kong, Q. & Huber, M. Regimes of soil moisture–wet-bulb temperature coupling with relevance to moist heat stress. *J. Clim.* **36**, 7925–7942 (2023).
30. Fischer, E. M., Oleson, K. W. & Lawrence, D. M. Contrasting urban and rural heat stress responses to climate change. *Geophys. Res. Lett.* **39**, 2011GL050576 (2012).
31. Huang, K. et al. Persistent increases in nighttime heat stress from urban expansion despite heat island mitigation. *J. Geophys. Res. Atmos.* **126**, e2020JD033831 (2021).
32. Sarangi, C. Urbanization amplifies nighttime heat stress on warmer days over the US. *Geophys. Res. Lett.* **48**, e2021GL095678 (2021).
33. Zhang, K. et al. Increased heat risk in wet climate induced by urban humid heat. *Nature* **617**, 738–742 (2023).
34. Tuholske, C. et al. Global urban population exposure to extreme heat. *Proc. Natl Acad. Sci. USA* **118**, e2024792118 (2021).
35. Zhong, S. et al. Urbanization-induced urban heat island and aerosol effects on climate extremes in the Yangtze River Delta region of China. *Atmos. Chem. Phys.* **17**, 5439–5457 (2017).
36. Debbage, N. & Shepherd, J. M. The urban heat island effect and city contiguity. *Comput. Environ. Urban Syst.* **54**, 181–194 (2015).
37. Qian, Y. et al. Urbanization impact on regional climate and extreme weather: current understanding, uncertainties, and future research directions. *Adv. Atmos. Sci.* <https://doi.org/10.1007/s00376-021-1371-9> (2022).
38. Chakraborty, T. C. et al. Urban versus lake impacts on heat stress and its disparities in a shoreline city. *GeoHealth* **7**, e2023GH000869 (2023).
39. Chakraborty, T. C. & Qian, Y. Urbanization exacerbates continental-to regional-scale warming. *One Earth* **7**, 1387–1401 (2024).
40. Wouters, H. et al. Soil drought can mitigate deadly heat stress thanks to a reduction of air humidity. *Sci. Adv.* **8**, eabe6653 (2022).
41. Vecellio, D. J., Kong, Q., Kenney, W. L. & Huber, M. Greatly enhanced risk to humans as a consequence of empirically determined lower moist heat stress tolerance. *Proc. Natl Acad. Sci. USA* **120**, e2305427120 (2023).
42. Wang, F., Gao, M., Liu, C., Zhao, R. & McElroy, M. B. Uniformly elevated future heat stress in China driven by spatially heterogeneous water vapor changes. *Nat. Commun.* **15**, 4522 (2024).
43. Lu, Y.-C. & Romps, D. M. Is a wet-bulb temperature of 35 °C the correct threshold for human survivability? *Environ. Res. Lett.* **18**, 094021 (2023).
44. Sherwood, S. C. & Huber, M. An adaptability limit to climate change due to heat stress. *Proc. Natl Acad. Sci. USA* **107**, 9552–9555 (2010).
45. Vecellio, D. J., Wolf, S. T., Cottle, R. M. & Kenney, W. L. Evaluating the 35 °C wet-bulb temperature adaptability threshold for young, healthy subjects (PSU HEAT Project). *J. Appl. Physiol.* **132**, 340–345 (2022).
46. Middel, A., Alkhaled, S., Schneider, F. A., Hagen, B. & Coseo, P. 50 Grades of Shade. *Bull. Am. Meteorol. Soc.* <https://doi.org/10.1175/BAMS-D-20-0193.1> (2021).
47. Lungman, T. et al. Cooling cities through urban green infrastructure: a health impact assessment of European cities. *Lancet* **401**, 577–589 (2023).

**Publisher's note** Springer Nature remains neutral with regard to jurisdictional claims in published maps and institutional affiliations.

Springer Nature or its licensor (e.g. a society or other partner) holds exclusive rights to this article under a publishing agreement with the author(s) or other rightsholder(s); author self-archiving of the accepted manuscript version of this article is solely governed by the terms of such publishing agreement and applicable law.

© Battelle Memorial Institute 2025

## Methods

### Model simulations

We use the Weather Research and Forecasting (WRF) model<sup>48</sup> version 3.8.1 with 4 km horizontal grids and a vertical resolution of 90 m nearest to the surface. The model is run with 64 vertical layers with a model top at 100 hPa. The WRF domain, covering most of North America east of the Rocky Mountains, is shown in Supplementary Fig. 1. The simulations are driven using initial and boundary conditions from the National Centers for Environment Prediction North American Regional Reanalysis product<sup>49</sup>. The Noah land surface model<sup>50</sup> with a single-layer canopy model<sup>51</sup> is used to represent urban surfaces. This implementation has three urban types with different density classes, that is, low-intensity residential (LIR), high-intensity residential (HIR) and commercial/industrial/transportation (CIT). We use the Defense Meteorological Satellite Program 1-km stable nighttime light product<sup>52</sup> to determine urban grids and their density class. Specifically, grid points with lighting index of 25–50, >50–58 and >58 are identified as LIR, HIR and CIT, respectively. For each urban class, urban fraction and thermal, radiative and morphological surface properties are prescribed (<https://github.com/wrf-model/WRF/blob/master/run/URBPARM.TBL>). Finally, anthropogenic heating, characterized by a diurnal cycle with two peaks at rush hours of 08:00 and 17:00 local standard time, is incorporated in the model simulations with maximum values of 20 W m<sup>-2</sup>, 50 W m<sup>-2</sup> and 90 W m<sup>-2</sup> for LIR, HIR and CIT, respectively<sup>53</sup>. An irrigation scheme is also included in the Noah land surface model to mimic sprinkler-type irrigation, the most common irrigation type in the United States, over the model domain. This is done by first incorporating a global map of potential irrigation areas (%) from the Food and Agriculture Organization<sup>54</sup> for each model grid and then combining that with the cropland and grassland grids, as defined by the International Geosphere-Biosphere Programme classification scheme in the Moderate Resolution Imaging Spectroradiometer (MODIS) land-cover dataset<sup>55</sup> to determine which grids will need irrigation. We assume that irrigation only happens during the growing season (April to October) when the root zone soil moisture availability (MA) is below a specific threshold. Here MA is defined as:

$$MA = \frac{SM - SM_{WP}}{SM_{FC} - SM_{WP}} \quad (2)$$

where SM, SM<sub>FC</sub> and SM<sub>WP</sub> are, respectively, the soil moisture content, soil moisture field capacity and soil moisture wilting point averaged for the entire soil column in Noah.

The growing season is defined when the green vegetation fraction (VF) is above the threshold (VF<sub>thresh</sub>) defined by:

$$VF_{thresh} = VF_{min} + 0.4 \times (VF_{max} - VF_{min}) \quad (3)$$

where VF<sub>max</sub> and VF<sub>min</sub> are the climatological maximum and minimum VF from the MODIS monthly estimates for each grid. During the growing season, MA is computed at 6:00 a.m. local time each day, and the irrigation is triggered when MA < 0.5. The daily amount of irrigation for the grid, which is distributed evenly during a 4-h time window between 6:00 a.m. and 10:00 a.m. local time, is the difference in the soil moisture holding capacity and current soil moisture content for the entire soil column in Noah multiplied by potential irrigation area<sup>2,15</sup>. Because the pervious fraction for the urban grids in the single-layer canopy model is treated as grassland, the irrigation scheme would also work for those grids, as long as the other conditions are satisfied. More details about the model configuration can be found in Sarangi et al.<sup>32</sup> and Li et al.<sup>6</sup>.

Three sets of WRF simulations are run, each initialized for 15 March and run until 1 September. The first set is the control or ‘no urban’ simulation, where the urban grids are replaced with the dominant nearby land-cover type. The second set of simulations (the ‘urban’ run) incorporated urban surfaces and anthropogenic heat flux<sup>32</sup>. The third set of

simulations (the ‘irrigation’ run) also includes the impact of irrigation throughout the model domain<sup>6</sup>. The first two simulations (‘no urban’ and ‘urban’ runs) do not include irrigation. The sets are initialized independently for each year between 2008 and 2012, together forming an ensemble of simulations. We focus our analysis on the summer period and thus only use model results for June, July and August for each year. We should note here that we do not have a fourth set of simulations with irrigation and no urbanization. This is because we treat the ‘urban’ case as the default and estimate the urban and irrigation impacts by adding and removing urbanization and irrigation, respectively.

### Generating urban clusters

The nightlights-derived urban surface dataset incorporated into the WRF model is also used to generate urban clusters in the model domain. This is done by first rasterizing the processed WRF surface dataset and then vectorizing contiguous urban grids into distinct urban clusters. This generates 1,662 clusters within the model (Extended Data Fig. 1). The location of the centroid of each cluster is used to determine the predominant Köppen–Geiger climate zone<sup>23</sup> that the cluster belongs to. On the basis of this analysis, there are 86, 605, 961 and 8 clusters in arid, boreal, temperate and tropical climate, respectively, within the model domain. Two of the 1,662 clusters have a mismatch with the extent of the Köppen–Geiger dataset and are not included in the climate zone analysis.

### Heat stress indices

We consider several indices to examine the impact of irrigation and urbanization on heat stress. This includes two operational indices, the heat index (HI), used by the US National Weather Service, and the Humidex, used by the Meteorological Service of Canada, the psychrometric or thermodynamic wet-bulb temperature (Tw), a measure of the adiabatic saturation temperature of air and a commonly used proxy for moist heat stress in the geosciences<sup>21,41,44</sup>, and the wet bulb globe temperature (WBGT)<sup>26</sup>, a comprehensive indicator of heat exposure that explicitly accounts for radiation and wind in addition to temperature and humidity.

The HI is calculated in multiple steps<sup>56</sup>. First, an initial HI estimate is made using an approximation of the Steadman<sup>57</sup> equation:

$$HI = 0.5 \times [T + 61 + [(T - 68) \times 1.2] + (0.094 RH)] \quad (4)$$

Here, T is in °F and RH is expressed as a percentage. If the average of this estimated HI and the value of T < 80 °F, this initial estimate is used as the final HI. If that average ≥ 80 °F, a more complex expression (equation (4)), the Rothfusz regression<sup>56</sup>, is used.

$$\begin{aligned} HI = & -42.379 + 2.04901523 \times T + 10.14333127 \times RH \\ & -0.22475541 \times T \times RH - 6.83783 \\ & \times 10^{-3} \times T^2 - 5.481717 \times 10^{-2} \times RH^2 \\ & + 1.22874 \times 10^{-3} \times T^2 \times RH + 8.5282 \\ & \times 10^{-4} \times T \times RH^2 - 1.99 \times 10^{-6} \times T^2 \times RH^2 \end{aligned} \quad (5)$$

Additional adjustments are made in the final value of HI for various humidity thresholds. For instance, when 80 °F ≤ T ≤ 112 °F and RH < 13%,  $(\frac{13-RH}{4})\sqrt{\frac{17-|T-95|}{17}}$  is subtracted from the original HI value. When RH > 85% and 80 °F ≤ T ≤ 87 °F,  $(\frac{RH-85}{10})(\frac{87-T}{5})$  is added to that original HI value.

Humidex is calculated using the following equation<sup>58</sup>:

$$Humidex = T + 0.5555 \times \left( 6.11 \times e^{5417.753 \times (\frac{1}{273.16} - \frac{1}{273.15+Td})} - 10 \right) \quad (6)$$

where Td is the dew-point temperature in °C.

The value of  $T_w$  is derived from iteratively solving the following expression, which is based on applying the leaf energy budget equation to a wet-bulb thermometer under adiabatic conditions<sup>59</sup>, and is an explicit function of  $T$  and the vapour pressure ( $e_v$ ):

$$T + \frac{1}{\gamma} e_v = T_w + \frac{1}{\gamma} e_{v^*}(T_w) \quad (7)$$

where  $\gamma$  is the psychrometric constant with a value of  $0.66 \text{ mb } ^\circ\text{C}^{-1}$  and  $e_{v^*}(T_w)$  is the saturation vapour pressure at  $T_w$ .

Finally, WBGT is calculated as a linear combination of  $T$ , the natural wet-bulb temperature ( $T_{nw}$ ), and the black-globe temperature ( $T_g$ )<sup>60</sup>.

$$\text{WBGT} = 0.1 \times T + 0.7 \times T_{nw} + 0.2 \times T_g \quad (8)$$

Equation (7) is for outdoor conditions. For indoor conditions, the WBGT reduces to:

$$\text{WBGT} = 0.7 \times T_{nw} + 0.3 \times T_g \quad (9)$$

To estimate  $T_g$ , we use the following equations<sup>61</sup> that explicitly account for the wind speed (WS) in  $\text{m s}^{-1}$  and solar radiation ( $K_\downarrow$ ) in  $\text{W m}^{-2}$ :

$$T_g = T - 0.3 + 0.0256 \times K_\downarrow - 0.18 \text{ WS}^{1/2} \quad (K_\downarrow \leq 400 \text{ W m}^{-2}) \quad (10)$$

$$T_g = T + 12.1 + 0.0067 \times K_\downarrow - 2.4 \text{ WS}^{1/2} \quad (K_\downarrow > 400 \text{ W m}^{-2}) \quad (11)$$

This method has the largest errors at the  $K_\downarrow$  discontinuity but performs well for high and low values of  $K_\downarrow$ <sup>61</sup>, which is what we focus on (next subsection). Unlike  $T_w$ ,  $T_{nw}$  is measured under real (usually non-adiabatic) conditions, which means it is also impacted by WS and  $K_\downarrow$ . So, we calculate  $T_{nw}$  from  $T_w$  based on a method used by Kestrel monitor manufacturers and previously used in the heat stress literature<sup>62</sup>, which accounts for WS and  $K_\downarrow$ . When  $T_g - T < 4$ :

$$T_{nw} = T - C \times (T - T_w) \quad (12)$$

$$C = 0.85 \quad (\text{WS} < 0.03 \text{ m s}^{-1}) \quad (13)$$

$$C = 1 \quad (\text{WS} > 3 \text{ m s}^{-1}) \quad (14)$$

$$C = 0.96 + 0.069 \log_{10} \text{WS} \quad (0.03 \text{ m s}^{-1} \leq \text{WS} \leq 3 \text{ m s}^{-1}) \quad (15)$$

When  $T_g - T \geq 4$ :

$$T_{nw} = T_w + 0.25 \times (T_g - T) + e \quad (16)$$

$$e = 1.1 \quad (\text{WS} < 0.1 \text{ m s}^{-1}) \quad (17)$$

$$e = -0.1 \quad (\text{WS} > 1 \text{ m s}^{-1}) \quad (18)$$

$$e = \frac{0.1}{\text{WS}^{1.1}} - 0.2 \quad (0.1 \text{ m s}^{-1} \leq \text{WS} \leq 1 \text{ m s}^{-1}) \quad (19)$$

When calculating indoor WBGT using equation (8),  $K_\downarrow$  and WS are set to zero when calculating  $T_g$  (in equations (9) and (10)).

Both HI and WBGT are now used operationally by the US NWS, and the heat risk categories used in most of this region<sup>63</sup> for both are shown in Fig. 1c,f. Given the variety of formulations, the difference in magnitude, and sometimes the direction, of irrigation impacts on all these different heat stress indices (main text) is a function of the various sensitivities of

these indices to the inputs, particularly humidity<sup>12,13,22</sup>. Of note, theoretical human adaptability limits of  $T_w$  have often been derived based on simple models for the human body<sup>44</sup>. This has prompted widespread use of  $T_w$  as a heat stress index in the geosciences<sup>10,17,21,33</sup>, even though  $T_w$  does not map well with heat strain compared to more operational heat stress indices<sup>27</sup>. More recently, Vecellio et al.<sup>45</sup> experimentally determined that heat stress can become uncompensable at lower thresholds of  $T_w$  in healthy adults, though these thresholds also depend on ambient vapour pressure. The upper adaptability limit for  $T_w$  of  $35^\circ\text{C}$  and the lowest limit found for warm-humid environments in Vecellio et al.<sup>45</sup> ( $30.34^\circ\text{C}$ ) are shown in Fig. 1e.

## Data processing

The hourly model outputs of each day are combined (averaged) to produce the composite diurnal cycles for summer for all five years (based on 460 days for the entire study period covering June, July and August of 2008 to 2012) and each year separately. Our analyses primarily focus on the average maximum (maximum of this averaged diurnal cycle) and average minimum (minimum of this averaged diurnal cycle) values of the variables. In addition to these variables, we estimate average WS,  $K_\downarrow$ , sensible heat flux ( $H$ ) and latent heat flux ( $\Lambda E$ ) and cloud fraction (CF; averaged over all vertical model layers) for each grid (Supplementary Fig. 2 and Extended Data Figs. 6 and 7). The differences between the ‘irrigation’ and ‘urban’ simulations are used to quantify the impacts of irrigation, while the difference between the ‘urban’ and ‘no urban’ simulations represent the urban impacts. In addition to the grid-wise estimates of changes, the model results are also aggregated into the 1,662 urban clusters. The cluster generation and spatial aggregation is done using the Google Earth Engine cloud computing platform<sup>64</sup>.

To examine the importance of different inputs on  $\text{WBGT}_{\max}$ , we use a multilinear equation.

$$\text{WBGT}_{\max} = \beta_0 + \beta_1 \times T + \beta_2 \times AH + \beta_3 \times WS + \beta_4 \times K_\downarrow \quad (20)$$

Within this linear framework,  $\beta_0$  is the intercept and  $\beta_1, \beta_2, \beta_3$  and  $\beta_4$  are the regression coefficients representing the sensitivity of the spatial distribution of  $\text{WBGT}_{\max}$  to the independent variables, with each data point being one grid in the model domain. AH is the absolute humidity, which we use here instead of RH because RH is also a function of  $T$ . In the main text, however, we mainly report the results on RH as it is a common meteorological variable and because it is directly used in most of the equations of moist heat stress. Because the independent variables in equation (19) have different ranges, we rescale all of them to lie between 0 and 1. Note that the values of  $T$ , AH, WS and  $K_\downarrow$  (here and in Figs. 4 and 6 and Extended Data Fig. 10) are for the times corresponding to the  $\text{WBGT}_{\max}$ , which do not necessarily correspond to their average maximum or average minimum (for AH) values. A similar equation can be written for  $\text{WBGT}_{\min}$ . Unlike  $\text{WBGT}_{\max}$ , which depends strongly on  $T$ , AH and  $K_\downarrow$  (main text), the spatial variability of  $\text{WBGT}_{\min}$  is mostly driven by  $T$ , with  $\beta_1, \beta_2, \beta_3$  and  $\beta_4$  of 0.90, 0.06, -0.7 and -0.07, respectively. Note that a negative regression coefficient for AH is found for the  $\text{WBGT}_{\max}$  model. This is not physically consistent, because all else remaining equal, an increase in AH will increase  $\text{WBGT}_{\max}$ . However, this is because there are confounding factors that simultaneously impact multiple variables in equation (19). While a known limitation of such parametric regression models, it is still useful here to interpret the relative importance of the inputs to WBGT.

## Validating impact of simulated irrigation on climate

We compare the model-simulated variables against reference data for both the regions common to the reference data and by climate zone to check how well the irrigation scheme improves model performance (Supplementary Fig. 2). For  $T_{\max}$ ,  $T_{\min}$ ,  $RH_{\max}$ ,  $RH_{\min}$ , WS and  $K_\downarrow$ , we use the GRIDMET dataset for the same period (June, July and August of 2008 to 2012) as the reference, which is available over continental

United States at 4 km resolution<sup>65</sup>. Because GRIDMET does not have  $H$  and  $\lambda E$ , which are strongly influenced by irrigation, we use the ERA5-Land reanalysis dataset<sup>66</sup> instead, which is available globally at roughly 9 km resolution. In both cases, we only choose the grids that are common to both model simulations and the reference dataset. For almost all the variables (except WS; Supplementary Fig. 2e), the irrigation scheme improves model performance compared to the reference data. There are some cases of degraded model performance, especially over tropical areas, but the irrigation scheme generally improves model accuracy. Of note, magnitudes of  $T$ , RH and  $K_1$  are well captured by the model, which gives us confidence in its ability to capture irrigation impacts on moist heat stress. Because these datasets do not resolve urban climate signals<sup>67</sup>, we do some additional evaluation by examining the variability in urban-scale average maximum and average minimum  $T$  using a recently released urban-resolving global 1 km dataset<sup>68</sup>. These comparisons are also made for northern hemisphere summer (June, July, August) for 2008 to 2012 (Supplementary Fig. 5). The overall variability in  $T_{\max}$  and  $T_{\min}$  across the 1,662 urban clusters is well captured by the model, with  $r^2$  values above 0.85 in all cases. The inclusion of irrigation reduces the positive mean bias error in  $T_{\max}$  and  $T_{\min}$  (Supplementary Fig. 5c), which is consistent with previous results on the role of irrigation in model biases in this region<sup>15</sup>. It is important to note that the validation is done as a sanity check against an independent estimate, and one would rarely expect complete agreement between the two datasets. We choose the Zhang et al.<sup>68</sup> dataset since it is the only urban-resolving dataset of its kind. However, it is not a true observational benchmark because it uses an empirical approach to link satellite-derived surface temperature to  $T$ , which can be tricky over urban areas<sup>22</sup>. These model simulations have also been independently evaluated in previous studies at the regional to domain scales<sup>6,32</sup>.

### Examining robustness of wet bulb globe temperature signals

Due to the lack of availability of all relevant model variables, we had to rely on certain empirical approximations when estimating the components of WBGT instead of using more direct formulations<sup>69</sup>. This would lead to some differences in the magnitude of the calculated WBGT. With that being said, the relevant question, in the context of the main results of this study, is whether the approximation would change the direction of the irrigation-induced WBGT signal. We have already demonstrated that irrigation generally reduces both HI and Humidex, two other moist heat stress indices that are more relevant to physiological impacts on humans than  $T_w$ <sup>27</sup>. To check the robustness of the irrigation signal for WBGT, we consider three other formulations that have been used in the geoscience heat stress literature. First, we recalculate  $T_w$  and then  $T_{nw}$  and WBGT using the formulation development by Stull<sup>70</sup>. This equation, given by,

$$\begin{aligned} T_w &= 273.15 + (T - 273.15) \times \text{atan}[0.151977(\text{RH} + 8.313659)^{1/2}] \\ &\quad + \text{atan}[(T - 273.15) + \text{RH}] - \text{atan}[\text{RH} - 1.676331] + 0.00391838(\text{RH})^{3/2} \\ &\quad \times \text{atan}[0.023101\text{RH}] - 4.686035 \end{aligned} \quad (21)$$

is also an approximation but has also been used in the recent heat stress literature<sup>14,17,42</sup>. We also consider two direct formulations of WBGT, one developed by Bernard and Iheanacho<sup>71</sup> for  $WBGT_{\max}$  and given by:

$$WBGT_{\max} = -0.0034\text{HI}_{\max}^2 + 0.96\text{HI}_{\max} - 34 \quad (22)$$

where  $\text{HI}_{\max}$  is in °F; and another by Ono and Tonouchi<sup>72</sup>:

$$\begin{aligned} WBGT &= 0.735 \times T + 0.0374 \times \text{RH} + 0.00292 \times T \times \text{RH} + 7.619 \times K_1 \\ &\quad - 4.557 \times K_1^2 - 0.0572 \times WS - 4.064 \end{aligned} \quad (23)$$

Both of these direct formulations have been used in other recent studies<sup>34,38,73</sup>, which allows us to contextualize the results of the present study within the existing scientific literature. For all four estimates of WBGT (Supplementary Fig. 6), irrigation reduces urban  $WBGT_{\max}$ , though there are some disagreements for tropical urban clusters, which we already treat with caution due to the small sample size.

### Limitations of model simulations

Regardless of the method used to estimate WBGT and other variables, it is important to keep in mind that these results are based on model simulations. Irrigation, for instance, is somewhat idealistic in our model simulations, and in reality, would be affected by both water demand, as considered here, and water availability and allocation and human decisions. For instance, when we compare the irrigation water use simulated by the model against reference irrigation water withdrawal data for 2015 from the US Geological Survey (Fig. 1)<sup>74</sup>, around an order of magnitude difference is seen between the two, even though the model captures the hotspot of irrigation water use within the domain (Supplementary Fig. 1b). However, this comparison has several limitations that would exaggerate the difference between the simulated and reference irrigation rate. First, the reference data are given as a daily average (mm per day) for a whole year (including cold season), while our simulations are only for the summer period, which is the growing season for several major crops in the region. Thus, we would expect summertime mean irrigation rate to be much higher than annual mean irrigation rate. Second, the reference data are developed by combining several data sources, many of which are static and from various distinct years. However, irrigation water use can change substantially from year to year depending on weather and climate conditions. Third, due to US Geological Survey restrictions on data release of individual farmers, the irrigation acre inputs used to generate the reference are expected to be biased low. There are several other uncertainties in the reference data that may lead to an underestimation of water use in the reference data. For instance, conveyance loss and irrigation efficiencies are not considered in many cases when producing that dataset but would still add to the surface water budget. Many of these uncertainties, some of them provided by state, are discussed in Painter et al.<sup>74</sup>. Given that reference data for seasonal irrigation are not available at sufficient spatial resolution, developing these datasets is critical so that future studies can better understand how 'real world' irrigation impacts the seasonality of the North American climate system. Although our simulated irrigation rate is most probably greater than 'real world' irrigation, there are diagnostic advantages of using a stronger perturbation to better separate the irrigation signal from the noise (internal variability) in coupled simulations. Overall, even if 'real world' irrigation rates were used in these simulations, we would not expect the sign of the moist heat stress signals to change.

Because these are fully coupled convection-permitting runs, the simulations can also be sensitive to initial conditions. To check for consistency of the key results, we calculate the percentage of the model grids where irrigation reduced moist heat stress (HI and Humidex) for the individual years, that is, for each member of the ensemble (Extended Data Fig. 10). Although the values are different across years, the simulations all consistently demonstrate that irrigation mostly reduces daytime moist heat stress in this region. Finally, these results are for agricultural irrigation and not urban-scale irrigation, which can vary widely between cities and can be quite different from irrigation in the background rural areas, particularly relevant for arid cities<sup>67</sup>.

### Data availability

The relevant variables from the model simulations and the processed data by urban cluster can be accessed via Zenodo at <https://doi.org/10.5281/zenodo.12522655> (ref. 75).

## Code availability

The code used for estimating the different heat stress indices can be accessed via Zenodo at <https://doi.org/10.5281/zenodo.12522655> (ref. 75).

## References

48. Skamarock, W. C. & Klemp, J. B. A time-split nonhydrostatic atmospheric model for weather research and forecasting applications. *J. Comput. Phys.* **227**, 3465–3485 (2008).
49. Mesinger, F. et al. North American regional reanalysis. *Bull. Am. Meteorol. Soc.* **87**, 343–360 (2006).
50. Chen, F. & Dudhia, J. Coupling an advanced land surface-hydrology model with the Penn State–NCAR MM5 modeling system. Part I: model implementation and sensitivity. *Mon. Weather Rev.* **129**, 569–585 (2001).
51. Kusaka, H., Kondo, H., Kikegawa, Y. & Kimura, F. A simple single-layer urban canopy model for atmospheric models: comparison with multi-layer and slab models. *Boundary Layer Meteorol.* **101**, 329–358 (2001).
52. Baugh, K., Elvidge, C. D., Ghosh, T. & Ziskin, D. Development of a 2009 stable lights product using DMSP-OLS data. *Proc. Asia-Pac. Adv. Netw.* **30**, 114 (2010).
53. Tewari, M., Chen, F., Kusaka, H. & Miao, S. Coupled WRF/Unified Noah/Urban-Canopy Modeling System NCAR WRF Doc. 122 (NCAR, 2007).
54. Siebert, S. et al. Development and validation of the global map of irrigation areas. *Hydrol. Earth Syst. Sci.* **9**, 535–547 (2005).
55. Strahler, A. in *MODIS Land Cover Product Algorithm Theoretical Basis Document (ATBD)*, v. 5.0 42–47 (NASA, 1999).
56. Rothfusz, L. P. in *The Heat Index Equation (or, More Than You Ever Wanted to Know About Heat Index)* 23–90 (NWS Southern Region, 1990).
57. Steadman, R. G. The assessment of sultriness. Part I: a temperature–humidity index based on human physiology and clothing science. *J. Appl. Meteorol. Climatol.* **18**, 861–873 (1979).
58. Masterton, J. M. & Richardson, F. A. *Humidex: A Method of Quantifying Human Discomfort Due to Excessive Heat and Humidity* (Environment Canada, Atmospheric Environment, 1979).
59. Lee, X. *Fundamentals of Boundary-Layer Meteorology*. Vol. 256 (Springer, 2018).
60. Yaglou, C. P. & Minard, D. Control of heat casualties at military training centers. *AMA Arch. Ind. Health* **16**, 302–316 (1957).
61. Okada, M. & Kusaka, H. Proposal of a new equation to estimate globe temperature in an urban park environment. *J. Agric. Meteorol.* **69**, 23–32 (2013).
62. Carter, A. W., Zaitchik, B. F., Gohlke, J. M., Wang, S. & Richardson, M. B. Methods for estimating wet bulb globe temperature from remote and low-cost data: a comparative study in Central Alabama. *GeoHealth* **4**, e2019GH000231 (2020).
63. Grundstein, A., Williams, C., Phan, M. & Cooper, E. Regional heat safety thresholds for athletics in the contiguous United States. *Appl. Geogr.* **56**, 55–60 (2015).
64. Gorelick, N. et al. Google Earth Engine: planetary-scale geospatial analysis for everyone. *Remote Sens. Environ.* **202**, 18–27 (2017).
65. Abatzoglou, J. T. Development of gridded surface meteorological data for ecological applications and modelling. *Int. J. Climatol.* **33**, 121–131 (2013).
66. Muñoz-Sabater, J. et al. ERA5-Land: a state-of-the-art global reanalysis dataset for land applications. *Earth Syst. Sci. Data* <https://doi.org/10.5194/essd-2021-82> (2021).
67. Chen, J., Qian, Y., Chakraborty, T. C. & Yang, Z. Complexities of urban impacts on long-term seasonal trends in a mid-sized arid city. *Environ. Res. Commun.* **6**, 021004 (2024).
68. Zhang, T. et al. A global dataset of daily maximum and minimum near-surface air temperature at 1 km resolution over land (2003–2020). *Earth Syst. Sci. Data* **14**, 5637–5649 (2022).
69. Liljegren, J. C., Carhart, R. A., Lawday, P., Tschoop, S. & Sharp, R. Modeling the wet bulb globe temperature using standard meteorological measurements. *J. Occup. Environ. Hyg.* **5**, 645–655 (2008).
70. Stull, R. Wet-bulb temperature from relative humidity and air temperature. *J. Appl. Meteorol. Climatol.* **50**, 2267–2269 (2011).
71. Bernard, T. E. & Iheanacho, I. Heat index and adjusted temperature as surrogates for wet bulb globe temperature to screen for occupational heat stress. *J. Occup. Environ. Hyg.* **12**, 323–333 (2015).
72. Ono, M. & Tonouchi, M. Estimation of wet-bulb globe temperature using generally measured meteorological indices. *Jpn. J. Biometeorol.* **50**, 147–157 (2014).
73. Ogata, S. et al. Heatstroke predictions by machine learning, weather information, and an all-population registry for 12-hour heatstroke alerts. *Nat. Commun.* **12**, 4575 (2021).
74. Painter, J. A., Brandt, J. T., Caldwell, R. R., Haynes, J. V. & Read, A. L. *Documentation of Methods and Inventory of Irrigation Information Collected for the 2015 US Geological Survey Estimated Use of Water in the United States* (United States Geological Survey, 2021).
75. Chakraborty, T. Data for irrigation impacts on urban heat stress in North America. Zenodo <https://doi.org/10.5281/zenodo.12522655> (2024).

## Acknowledgements

Pacific Northwest National Laboratory is operated for the US Department of Energy (DOE) by Battelle Memorial Institute under contract DE-AC05-76RL01830. This study is supported by the Integrated Coastal Modeling (ICoM) project, a multi-institutional project supported by DOE's Office of Science's Office of Biological and Environmental Research as part of the Earth and Environmental Systems Modeling programme and a DOE Early Career award to T.C. We thank J. Deines for the discussions on available reference irrigation water use datasets.

## Author contributions

T.C. processed the data and wrote the paper. J.L. and C.S. ran the model simulations. Y.Q. and L.R.L. provided inputs on experimental design. All authors contributed to writing and revision.

## Competing interests

The authors declare no competing interests.

## Additional information

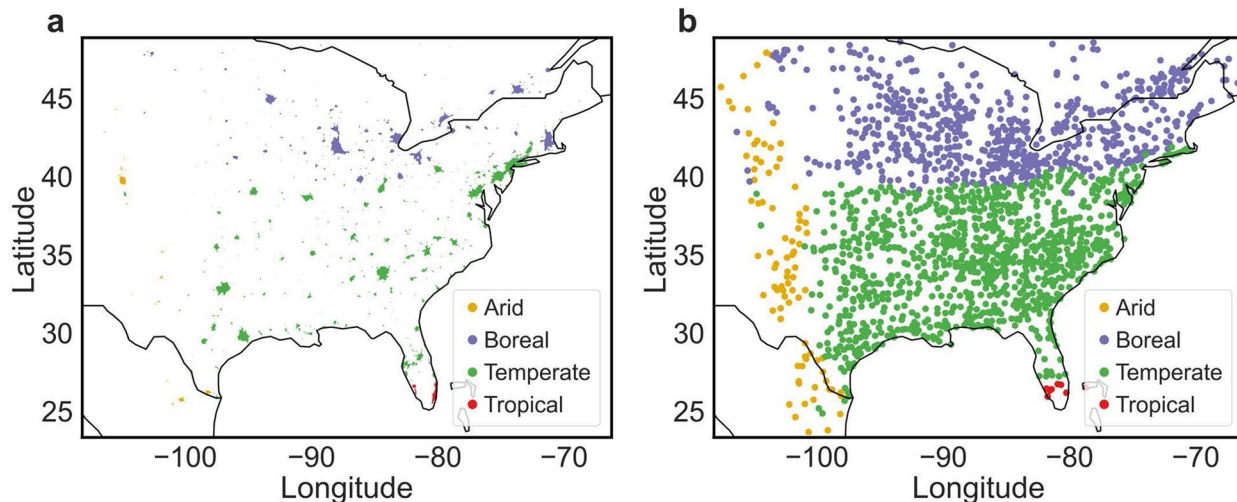
**Extended data** is available for this paper at <https://doi.org/10.1038/s41561-024-01613-z>.

**Supplementary information** The online version contains supplementary material available at <https://doi.org/10.1038/s41561-024-01613-z>.

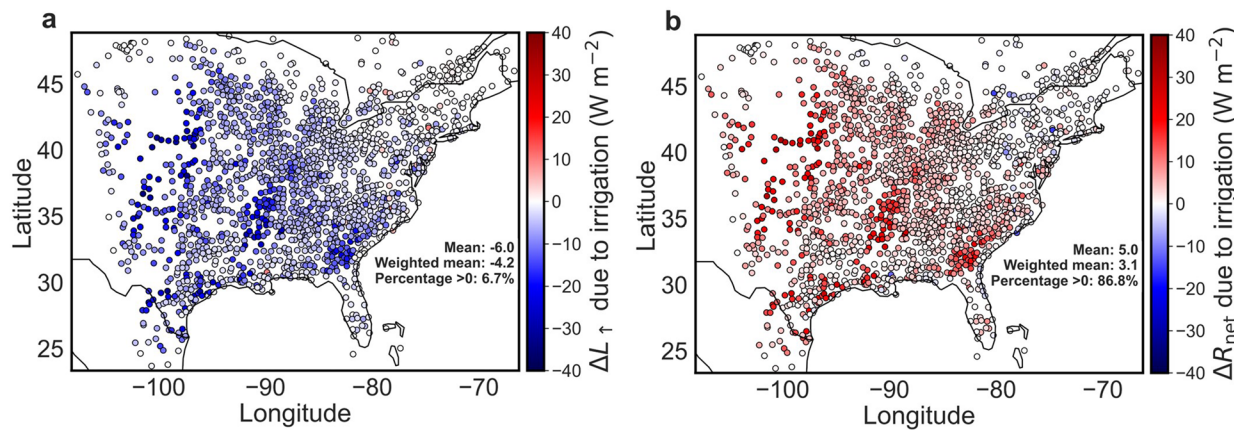
**Correspondence and requests for materials** should be addressed to TC Chakraborty or Yun Qian.

**Peer review information** *Nature Geoscience* thanks Qinjin Kong, Yadu Pokhrel and the other, anonymous, reviewer(s) for their contribution to the peer review of this work. Primary Handling Editor: Tom Richardson, in collaboration with the *Nature Geoscience* team.

**Reprints and permissions information** is available at [www.nature.com/reprints](http://www.nature.com/reprints).

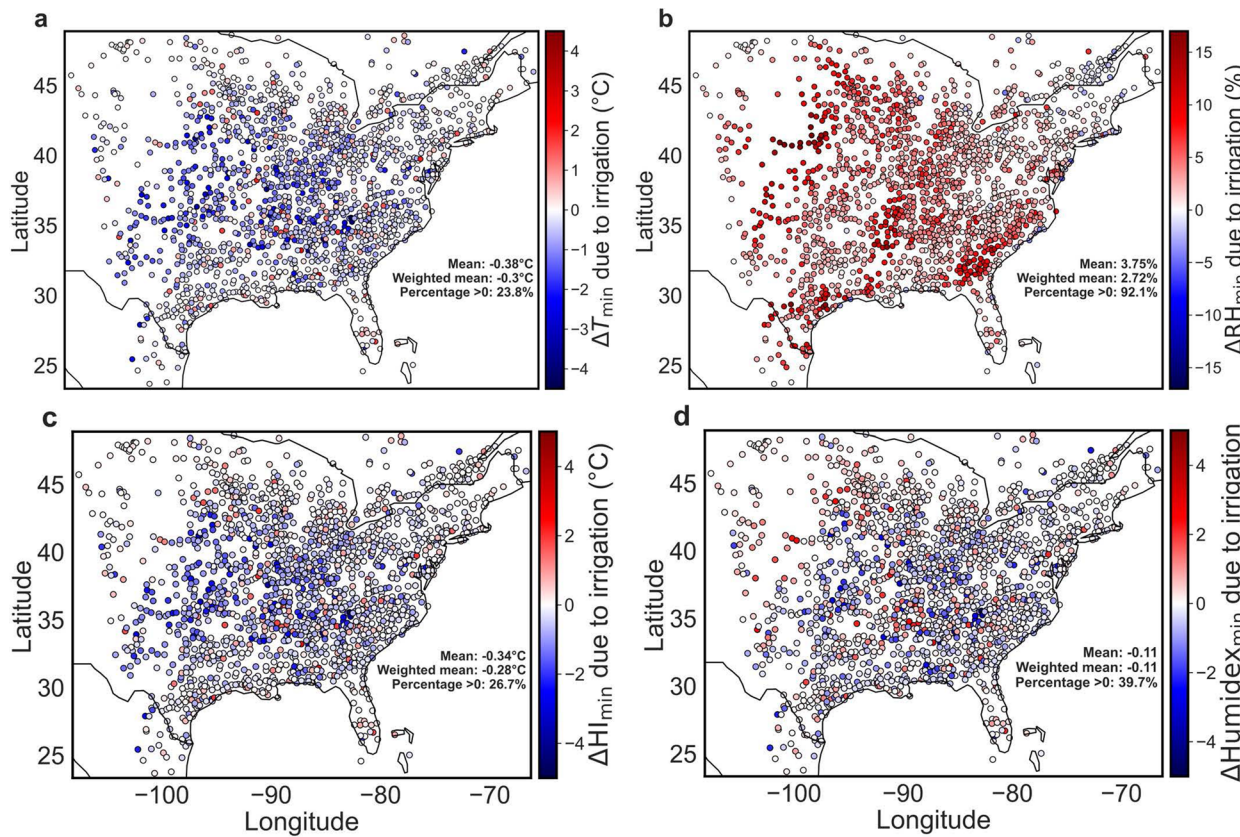


**Extended Data Fig. 1 | Generated urban clusters for region of interest.** Sub-figure **a** shows the location, extent, and background Köppen-Geiger climate zone of all 1662 urban clusters generated in the region of interest from the model's surface dataset. Sub-figure **b** is similar to **a**, but shows the centroids of the clusters instead of their extent for easier visibility.



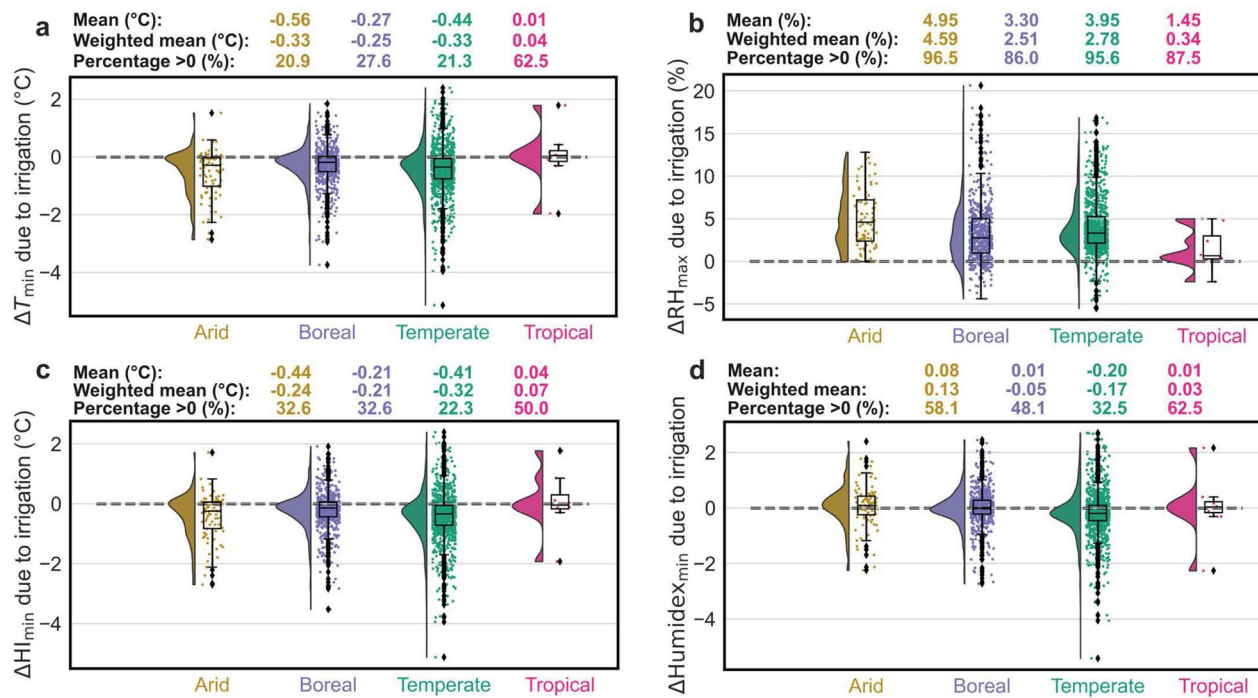
**Extended Data Fig. 2 | Changes in mean outgoing longwave radiation and net radiation over urban clusters due to irrigation.** Urban-scale irrigation-induced changes in mean **a** outgoing longwave radiation ( $\Delta L$ ), and **b** net radiation ( $\Delta R_{\text{net}}$ )

due to irrigation for every urban cluster. Each dot represents the spatial mean for an urban cluster. The urban spatial means, area-weighted spatial means, and percentage of urban clusters with values above 0 are also noted.



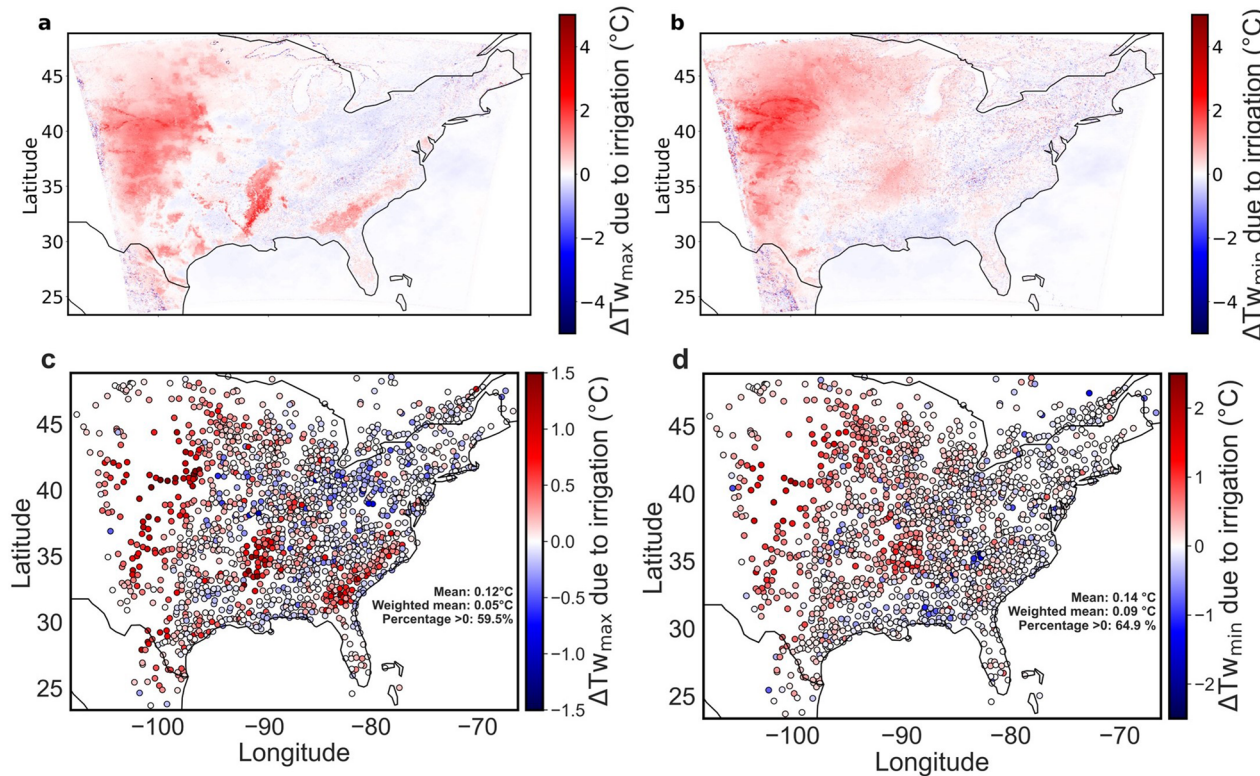
**Extended Data Fig. 3 | Changes in nighttime urban climate and moist heat stress due to irrigation.** Urban-scale irrigation-induced changes in **a** minimum air temperature ( $\Delta T_{\min}$ ), **b** maximum relative humidity ( $\Delta RH_{\max}$ ), **c** minimum heat index ( $\Delta HI_{\min}$ ), and **d** minimum Humidex ( $\Delta \text{Humidex}_{\min}$ ) due to irrigation for

every urban cluster. Each dot represents the spatial mean for an urban cluster. The urban spatial means, area-weighted spatial means, and percentage of urban clusters with values above 0 are also noted.



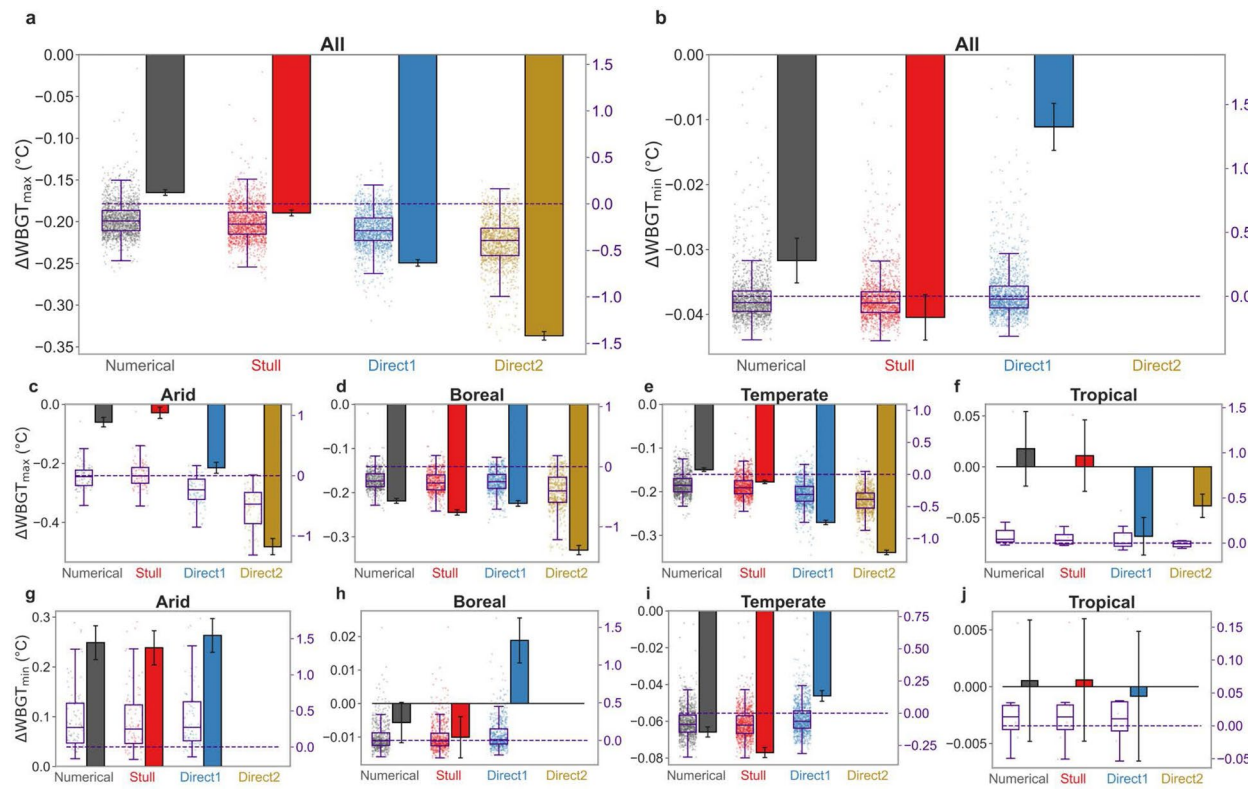
**Extended Data Fig. 4 | Irrigation impacts on nighttime urban climate and moist heat stress across climate zones.** Distribution of irrigation-induced changes in **a** minimum air temperature ( $\Delta T_{\min}$ ), **b** maximum relative humidity ( $\Delta RH_{\max}$ ), **c** minimum heat index ( $\Delta HI_{\min}$ ), and **d** minimum Humidex ( $\Delta \text{Humidex}_{\min}$ ) for every urban cluster in the model domain by climate zone. The

means, area-weighted means, and percentage of urban clusters with values above 0 are noted for each case. Each dot represents the spatial mean for an urban cluster. The number of clusters in arid, boreal, temperate, and tropical climate are 86, 605, 961, and 8, respectively.


**Extended Data Fig. 5 | Changes in psychrometric wet-bulb temperature.**

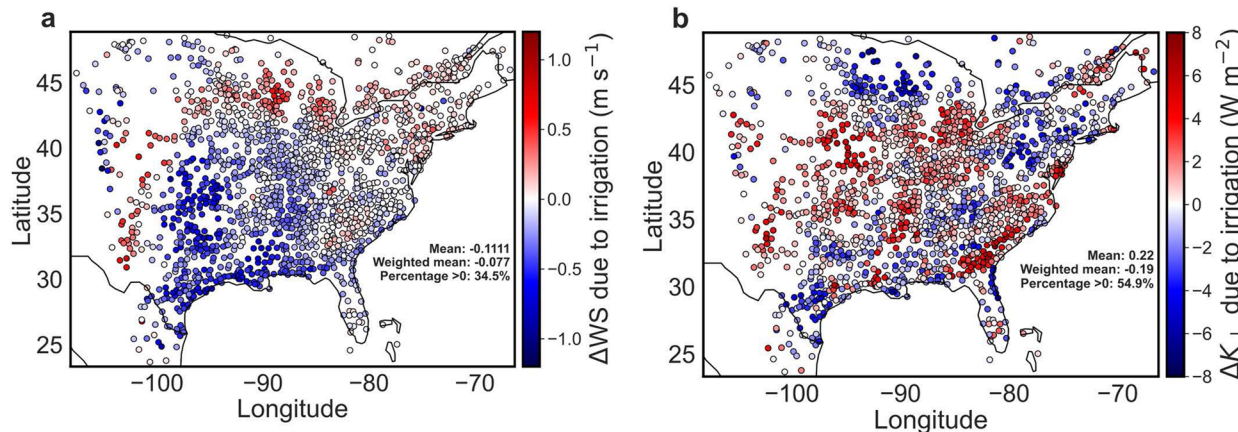
Irrigation-induced grid-wise changes in **a** maximum and, **b** minimum psychrometric wet-bulb temperature ( $\Delta Tw_{\max}$  and  $\Delta Tw_{\min}$ , respectively) over the model domain. Sub-figures **c** and **d** are similar to **a** and **b**, but for urban-scale

changes. Each **c** and **d**, each dot represents the spatial mean for an urban cluster. The urban spatial means, area-weighted spatial means, and percentage of urban clusters with values above 0 are also noted for these.



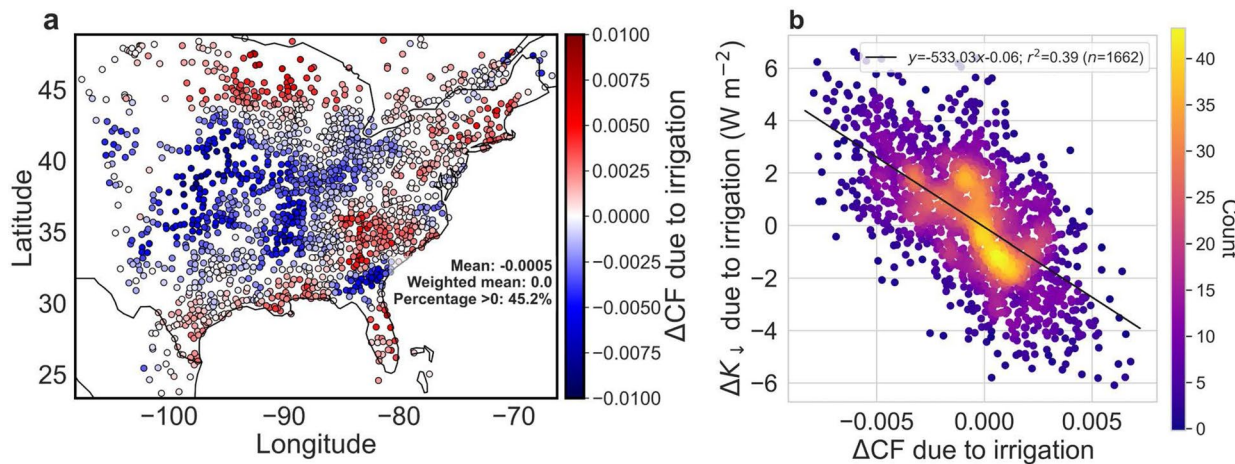
**Extended Data Fig. 6 | Consistency in irrigation-induced outdoor wet bulb globe temperature signals.** Irrigation-induced changes in average **a** maximum and **b** minimum outdoor wet bulb globe temperature ( $\Delta\text{WBGT}_{\max}$  and  $\Delta\text{WBGT}_{\min}$ , respectively) in urban clusters. Sub-figures **c**, **d**, **e**, and **f** are similar to **a** (for  $\Delta\text{WBGT}_{\max}$ ), but for arid, boreal, temperate, and tropical urban clusters, respectively. Similarly, sub-figures **g**, **h**, **i**, and **j** are for  $\Delta\text{WBGT}_{\min}$  by climate zone. Different methodologies are used to estimate WBGT, including the numerical method used in the main text, WBGT derived from the wet-bulb temperature

values based on Stull, and two direct equations (Direct1 and Direct2). See Methods for more details. The bars represent area-weighted means and the error bars show area-weighted standard errors. The distributions of the cluster-level data and the associated box and whisker plots correspond to the right-hand y axis range. The number of clusters in arid, boreal, temperate, and tropical climate are 86, 605, 961, and 8, respectively. The boxes range from the first to third quartile of the subsets of data, with the median marked by a line. The whiskers extend to 1.5 times the interquartile ranges of the boxes.



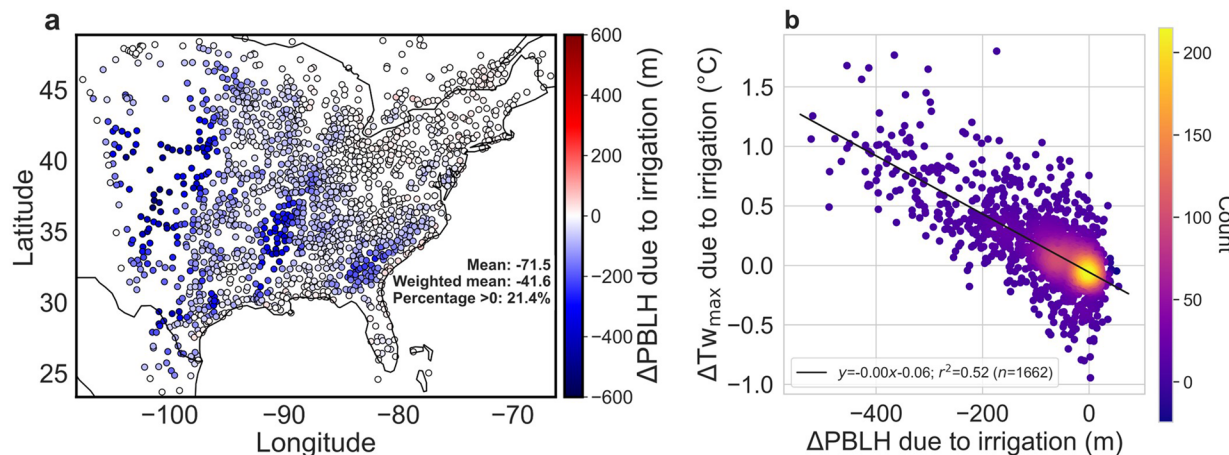
**Extended Data Fig. 7 | Changes in wind speed and incoming shortwave radiation due to irrigation.** Urban-scale irrigation-induced changes in **a** average wind speed ( $\Delta W_S$ ), and **b** incoming shortwave radiation ( $\Delta K_s$ ) for every urban

cluster in the model domain. Each dot represents the spatial mean for an urban cluster. The urban spatial means, area-weighted spatial means, and percentage of urban clusters with values above 0 are also noted.



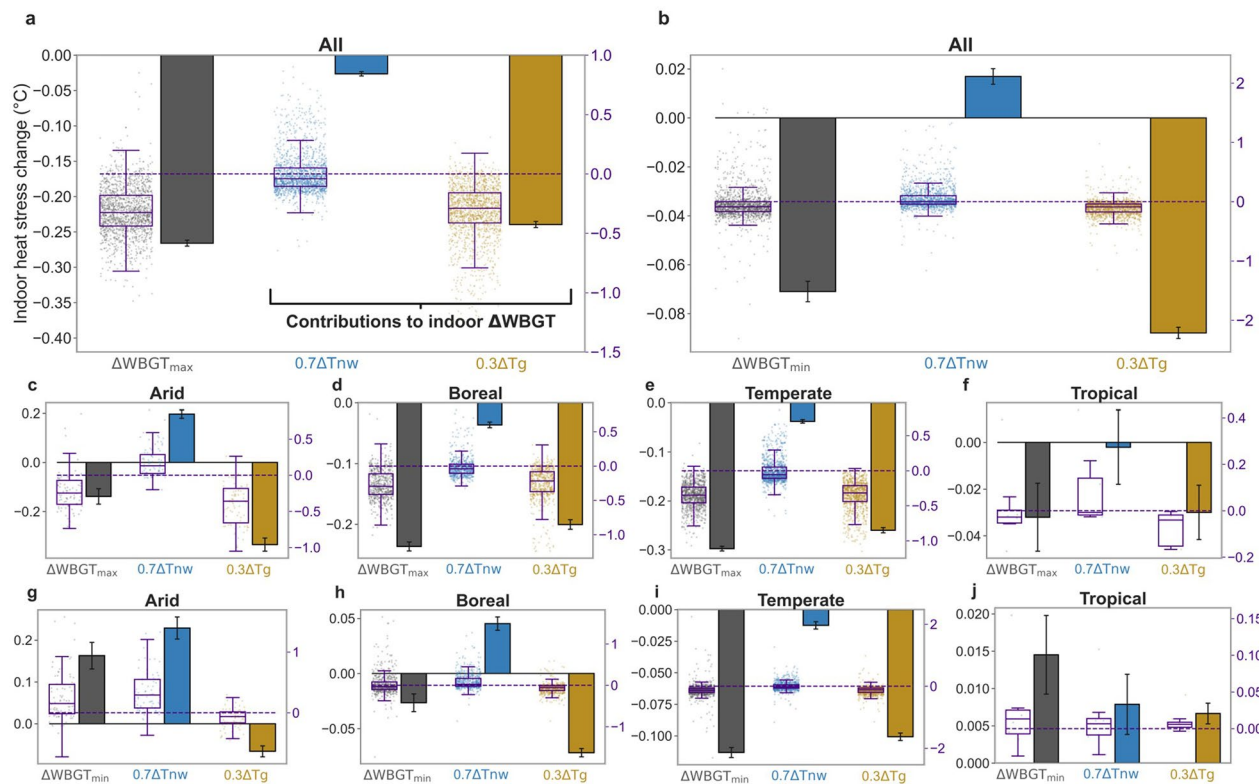
**Extended Data Fig. 8 | Changes in cloud cover due to irrigation and its control on incoming shortwave radiation change.** Urban-scale irrigation-induced changes in average cloud fraction ( $\Delta\text{CF}$ ) for every urban cluster in the model domain. Each dot represents the spatial mean for an urban cluster. The urban spatial means, area-weighted spatial means, and percentage of urban clusters

with values above 0 are also noted. Sub-figure **b** shows associations between the irrigation-induced change in incoming shortwave radiation ( $\Delta K_{\downarrow}$ ) and  $\Delta\text{CF}$ . Each data point is one urban cluster. The lines of best fit and the coefficient of determination ( $r^2$ ) is noted. The color indicates the density of data points.



**Extended Data Fig. 9 | Changes in planetary boundary layer height due to irrigation and its control on wet-bulb temperature change.** Urban-scale irrigation-induced changes in average planetary boundary layer height ( $\Delta\text{PBLH}$ ) for every urban cluster in the model domain. Each dot represents the spatial mean for an urban cluster. The urban spatial means, area-weighted spatial

means, and percentage of urban clusters with values above 0 are also noted. Sub-figure **b** shows associations between the irrigation-induced change in maximum psychrometric wet-bulb temperature ( $\Delta\text{Tw}_{\text{max}}$ ) and  $\Delta\text{PBLH}$ . Each data point is one urban cluster. The lines of best fit and the coefficient of determination ( $r^2$ ) is noted. The color indicates the density of data points.



**Extended Data Fig. 10 | Changes in urban indoor wet bulb globe temperature and its components due to irrigation.** Irrigation-induced changes in average **a** maximum and **b** minimum indoor wet bulb globe temperature ( $\Delta\text{WBGT}_{\text{max}}$  and  $\Delta\text{WBGT}_{\text{min}}$ , respectively) in urban clusters. Sub-figures **c**, **d**, **e**, and **f** are similar to **a** (for  $\Delta\text{WBGT}_{\text{max}}$ ), but for arid, boreal, temperate, and tropical urban clusters, respectively. Similarly, sub-figures **g**, **h**, **i**, and **j** are for  $\Delta\text{WBGT}_{\text{min}}$  by climate zone. The contributions of change in natural wet-bulb temperature ( $\Delta\text{Tnw}$ ), and black-

globe temperature ( $\Delta\text{Tg}$ ) are shown. The bars represent area-weighted means and the error bars show area-weighted standard errors. The distributions of the cluster-level data and the associated box and whisker plots correspond to the right-hand y axis range. The number of clusters in arid, boreal, temperate, and tropical climate are 86, 605, 961, and 8, respectively. The boxes range from the first to third quartile of the subsets of data, with the median marked by a line. The whiskers extend to 1.5 times the interquartile ranges of the boxes.

## Terms and Conditions

Springer Nature journal content, brought to you courtesy of Springer Nature Customer Service Center GmbH (“Springer Nature”). Springer Nature supports a reasonable amount of sharing of research papers by authors, subscribers and authorised users (“Users”), for small-scale personal, non-commercial use provided that all copyright, trade and service marks and other proprietary notices are maintained. By accessing, sharing, receiving or otherwise using the Springer Nature journal content you agree to these terms of use (“Terms”). For these purposes, Springer Nature considers academic use (by researchers and students) to be non-commercial.

These Terms are supplementary and will apply in addition to any applicable website terms and conditions, a relevant site licence or a personal subscription. These Terms will prevail over any conflict or ambiguity with regards to the relevant terms, a site licence or a personal subscription (to the extent of the conflict or ambiguity only). For Creative Commons-licensed articles, the terms of the Creative Commons license used will apply.

We collect and use personal data to provide access to the Springer Nature journal content. We may also use these personal data internally within ResearchGate and Springer Nature and as agreed share it, in an anonymised way, for purposes of tracking, analysis and reporting. We will not otherwise disclose your personal data outside the ResearchGate or the Springer Nature group of companies unless we have your permission as detailed in the Privacy Policy.

While Users may use the Springer Nature journal content for small scale, personal non-commercial use, it is important to note that Users may not:

1. use such content for the purpose of providing other users with access on a regular or large scale basis or as a means to circumvent access control;
2. use such content where to do so would be considered a criminal or statutory offence in any jurisdiction, or gives rise to civil liability, or is otherwise unlawful;
3. falsely or misleadingly imply or suggest endorsement, approval , sponsorship, or association unless explicitly agreed to by Springer Nature in writing;
4. use bots or other automated methods to access the content or redirect messages
5. override any security feature or exclusionary protocol; or
6. share the content in order to create substitute for Springer Nature products or services or a systematic database of Springer Nature journal content.

In line with the restriction against commercial use, Springer Nature does not permit the creation of a product or service that creates revenue, royalties, rent or income from our content or its inclusion as part of a paid for service or for other commercial gain. Springer Nature journal content cannot be used for inter-library loans and librarians may not upload Springer Nature journal content on a large scale into their, or any other, institutional repository.

These terms of use are reviewed regularly and may be amended at any time. Springer Nature is not obligated to publish any information or content on this website and may remove it or features or functionality at our sole discretion, at any time with or without notice. Springer Nature may revoke this licence to you at any time and remove access to any copies of the Springer Nature journal content which have been saved.

To the fullest extent permitted by law, Springer Nature makes no warranties, representations or guarantees to Users, either express or implied with respect to the Springer nature journal content and all parties disclaim and waive any implied warranties or warranties imposed by law, including merchantability or fitness for any particular purpose.

Please note that these rights do not automatically extend to content, data or other material published by Springer Nature that may be licensed from third parties.

If you would like to use or distribute our Springer Nature journal content to a wider audience or on a regular basis or in any other manner not expressly permitted by these Terms, please contact Springer Nature at

[onlineservice@springernature.com](mailto:onlineservice@springernature.com)